Neurobiology of Disease

Lower Affinity of Isradipine for L-Type Ca^{2+} Channels during Substantia Nigra Dopamine Neuron-Like Activity: Implications for Neuroprotection in Parkinson's Disease

Nadine J. Ortner,[1] Gabriella Bock,[1] Antonios Dougalis,[4] Maria Kharitonova,[1] Johanna Duda,[4] Simon Hess,[6] Petronel Tuluc,[1] Thomas Pomberger,[1] Nadia Stefanova,[2] Florian Pitterl,[3] Thomas Ciossek,[5] Herbert Oberacher,[3] Henning J. Draheim,[5] Peter Kloppenburg,[6] Birgit Liss,[4] and Jörg Striessnig[1]

[1]Department of Pharmacology and Toxicology, Center for Molecular Biosciences, University of Innsbruck, 6020 Innsbruck, Austria, [2]Department of Neurology and [3]Institute of Legal Medicine and Core Facility Metabolomics, Medical University of Innsbruck, 6020 Innsbruck, Austria, [4]Institute of Applied Physiology, University of Ulm, 89081 Ulm, Germany, [5]Boehringer Ingelheim Pharma GmbH & Co KG, CNS Research, 88400 Biberach an der Riss, Germany, and [6]Biocenter, Institute for Zoology, and Cologne Excellence Cluster on Cellular Stress Responses in Aging-Associated Diseases (CECAD), University of Cologne, 50674 Cologne, Germany

Ca^{2+}-influx through L-type Ca^{2+}-channels (LTCCs) is associated with activity-related stressful oscillations of Ca^{2+} levels within dopaminergic (DA) neurons in the substantia nigra (SN), which may contribute to their selective degeneration in Parkinson's disease (PD). LTCC blockers were neuroprotective in mouse neurotoxin models of PD, and isradipine is currently undergoing testing in a phase III clinical trial in early PD. We report no evidence for neuroprotection by *in vivo* pretreatment with therapeutically relevant isradipine plasma levels, or $Ca_v1.3$ LTCC deficiency in 6-OHDA-treated male mice. To explain this finding, we investigated the pharmacological properties of human LTCCs during SN DA-like and arterial smooth muscle (aSM)-like activity patterns using whole-cell patch-clamp recordings in HEK293 cells ($Ca_v1.2$ α1-subunit, long and short $Ca_v1.3$ α1-subunit splice variants; $\beta3/\alpha2\delta1$). During SN DA-like pacemaking, only $Ca_v1.3$ variants conducted Ca^{2+} current (I_{Ca}) at subthreshold potentials between action potentials. SN DA-like burst activity increased integrated I_{Ca} during ($Ca_v1.2$ plus $Ca_v1.3$) and after ($Ca_v1.3$) the burst. Isradipine inhibition was splice variant and isoform dependent, with a 5- to 11-fold lower sensitivity to $Ca_v1.3$ variants during SN DA-like pacemaking compared with $Ca_v1.2$ during aSM-like activity. Supratherapeutic isradipine concentrations reduced the pacemaker precision of adult mouse SN DA neurons but did not affect their somatic Ca^{2+} oscillations. Our data predict that $Ca_v1.2$ and $Ca_v1.3$ splice variants contribute differentially to Ca^{2+} load in SN DA neurons, with prominent $Ca_v1.3$-mediated I_{Ca} between action potentials and after bursts. The failure of therapeutically relevant isradipine levels to protect SN DA neurons can be explained by weaker state-dependent inhibition of SN DA LTCCs compared with aSM $Ca_v1.2$.

Key words: calcium; isradipine; L-type calcium channels; neuroprotection; Parkinson's disease; pharmacology

Significance Statement

The high vulnerability of dopamine (DA) neurons in the substantia nigra (SN) to neurodegenerative stressors causes Parkinson's disease (PD). Ca^{2+} influx through voltage-gated L-type Ca^{2+} channels (LTCCs), in particular $Ca_v1.3$, appears to contribute to this vulnerability, and the LTCC inhibitor isradipine is currently being tested as a neuroprotective agent for PD in a phase III clinical trial. However, in our study isradipine plasma concentrations approved for therapy were not neuroprotective in a PD mouse model. We provide an explanation for this observation by demonstrating that during SN DA-like neuronal activity LTCCs are less sensitive to isradipine than $Ca_v1.2$ LTCCs in resistance blood vessels (mediating dose-limiting vasodilating effects) and even at supratherapeutic concentrations isradipine fails to reduce somatic Ca^{2+} oscillations of SN DA neurons.

Introduction

Parkinson's disease (PD) is a neurodegenerative movement disorder, and existing therapies are neither curative nor neuroprotective. The primary motor symptoms reflect the progressive loss of dopaminergic (DA) neurons, particularly within the substantia nigra (SN; Hurley and Dexter, 2012; Sulzer and Surmeier,

Received Sept. 16, 2016; revised May 8, 2017; accepted May 13, 2017.

Author contributions: N.J.O., G.B., S.H., P.T., N.S., H.O., P.K., B.L., and J.S. designed research; N.J.O., G.B., A.D., M.K., J.D., S.H., T.P., and F.P. performed research; T.C. and H.J.D. contributed unpublished reagents/analytic tools; N.J.O., G.B., A.D., M.K., J.D., S.H., P.T., N.S., F.P., H.O., P.K., B.L., and J.S. analyzed data; N.J.O., P.K., B.L., and J.S. wrote the paper.

This work was supported by the Austrian Science Fund (Grants F4402, F4412, W1101-B12, and P27809), the Deutsche Forschungsgemeinschaft (Grants Li1754/1 and SFB1218/TPB07), the Alfried Krupp von Bohlen und Halbach Foundation, the Medical University of Innsbruck, and the University of Innsbruck. We thank Bruno Benedetti and Andreas Lieb for providing the murine SN DA command voltage; Gerald Obermair for helpful comments on statistics; Stephan Geley for generously providing the pTO HA strepIII C GW FRT and pOG44 vectors and expertise for

2013). These neurons constantly fire action potentials (APs; Grace and Bunney, 1984a,b; Puopolo et al., 2007), resulting in an oscillatory Ca^{2+} influx throughout the dendrites and the soma (Chan et al., 2007). The metabolically challenging task to remove Ca^{2+} from the cytosol increases SN DA mitochondrial oxidative stress (Guzman et al., 2009, 2010), rendering them more vulnerable to degeneration (for reviews see Surmeier et al., 2012; Duda et al., 2016).

L-type voltage-gated Ca^{2+} channels [LTCCs (Ca_v1); Catterall et al., 2005] are required for normal endocrine, brain, sensory, and muscle function (Hofmann et al., 2014; Striessnig et al., 2014), and brain $Ca_v1.2$ and $Ca_v1.3$ channels are also expressed by SN DA neurons (Olson et al., 2005; Dragicevic et al., 2014; Philippart et al., 2016; Sun et al., 2017). $Ca_v1.3$ channels can open at subthreshold membrane potentials due to their negative activation voltage range (Koschak et al., 2001; Xu and Lipscombe, 2001; Lieb et al., 2014) and are thus postulated to be a major contributor to mitochondrial stress-inducing Ca^{2+} oscillations in SN DA neurons (Surmeier et al., 2011; Hurley and Dexter, 2012; Hurley et al., 2013; Sulzer and Surmeier, 2013; Branch et al., 2014). Reducing LTCC activity using specific blockers is currently being pursued as a new neuroprotective strategy (Surmeier et al., 2011).

Dihydropyridine (DHP) channel blockers have a long history of safe use as antihypertensive agents due to their potent inhibition of $Ca_v1.2$ currents in arterial smooth muscle (aSM; Moosmang et al., 2003; Zhang et al., 2007). DHP channel blockers are nonselective, blocking both $Ca_v1.2$ and $Ca_v1.3$ channels (Koschak et al., 2001; Xu and Lipscombe, 2001). $Ca_v1.3$-selective blockers would avoid $Ca_v1.2$-mediated cardiovascular side effects but are unestablished (Kang et al., 2012; Huang et al., 2014; Ortner et al., 2014). Although human epidemiological studies indicate a 20–30% lower risk of the development of PD in patients treated with nonselective brain-permeant DHP channel blockers (Striessnig et al., 2014 for references), preclinical *in vivo* studies with DHP channel blockers in PD animal models are controversial. For example, several studies report DHP-mediated protection of SN DA neurons (Kupsch et al., 1995, 1996; Chan et al., 2007; Meredith et al., 2008; Ilijic et al., 2011), but others have failed to confirm these findings (Sautter et al., 1997). Although differences in experimental design may explain some of these discrepancies, it remains unclear whether brain $Ca_v1.2$ and $Ca_v1.3$ channels are inhibited as effectively as aSM $Ca_v1.2$ channels at doses of DHP channel blockers used for chronic DHP treatment. This question is of particular relevance in light of an ongoing phase III clinical trial (NCT02168842) investigating the neuroprotective effect of the nonselective DHP compound, isradipine (ISR), in early PD patients.

In this study, we find that neither treatment with human therapeutic plasma levels of ISR nor global $Ca_v1.3$ deficiency in a 6-hydroxydopamine (6-OHDA) PD mouse model provides neuroprotection. To explore the possibility that ISR, due to its known state-dependent block of LTCCs, is a weaker blocker of brain LTCCs compared with their therapeutic targets in aSM, we compared the LTCC ISR sensitivity of human $Ca_v1.2$ and $Ca_v1.3$ channels stably expressed in HEK293 cells using whole-cell patch-clamp recordings applying aSM-like and SN DA-like command voltages. LTCCs during SN DA activity, especially $Ca_v1.3$ variants, required higher concentrations of ISR for inhibition (4.6- to 11.2-fold for $Ca_v1.3$ splice variants) than aSM $Ca_v1.2$. Moreover, we show that pacemaker activity and related somatic Ca^{2+} oscillations of SN DA neurons from adult mouse brain slices were not significantly inhibited even at supratherapeutic ISR concentrations (30 nM), supporting our prediction of lower ISR sensitivity of $Ca_v1.3$ channels, and explaining the absence of neuroprotective effects in the 6-OHDA PD model. Our data predict that $Ca_v1.3$-mediated neuroprotection in humans would require supratherapeutic doses of ISR, which are unlikely to be tolerated during long-term treatment.

Materials and Methods

Animals

All animal experiments were approved by the Austrian Animal Experimentation Ethics Board (BMWF-66.008/0026-II/3b/2011), by the German Regierungspräsidium Tübingen (AZ 35/9185.81–3. TV1043, Regulation no. 0.147), or by the LANUV NRW, Recklinghausen, Germany (84-02.05. 20.12.254). Male C57BL/6, 12–15 weeks of age, wild-type or age-matched $Ca_v1.3$ knock-out mice ($Ca_v1.3^{-/-}$; RRID:MGI:218788; Platzer et al., 2000) were used. For quantitative real-time PCR (qRT-PCR) experiments, male C57BL/6 mice [postnatal day 13 (P13) and ~P90] were used and bred in the animal facility of the Ulm University.

Unilateral 6-hydroxydopamine lesions

Striatal unilateral 6-OHDA lesions were induced by a single vertical stereotactic injection of 6-OHDA (catalog #162957, Sigma-Aldrich; dissolved in 0.2% saline with 0.02% ascorbic acid) at a rate of 0.1 μl/min into the dorsal striatum (anteroposterior, −0.4 mm; mediolateral, +1.8 mm; dorsoventral, +2.9 mm; Paxinos and Franklin, 2001). 6-OHDA caused a dose-dependent loss of tyrosine hydroxylase-positive (TH^+) SN DA neurons [remaining cells, percentage of nonlesioned side (mean ± SEM): 1.7 μg: 69.2 ± 4.2%, $n = 14$; 4.1 μg: 50.5 ± 3.3%, $n = 51$] compared with injections of vehicle alone (95.2 ± 1.3%, $n = 10$). A total of 4.1 μg of 6-OHDA (in 1 μl) was therefore chosen for evaluating the neuroprotective effects of ISR or of $Ca_v1.3$ deficiency 28 d after lesioning. Surviving SN DA neurons were visualized by TH immunohistochemical staining of brain slices (40 μm) using mouse anti-TH (diluted 1:1000; catalog #T2928, Sigma-Aldrich) as primary antibody and a biotinylated donkey anti-mouse secondary antibody (dilution 1:200, Jackson ImmunoResearch). The number of TH^+ SN DA neurons in the lesioned and nonlesioned (control) sides were quantified by unbiased stereological analysis using the optical fractionator method with a Nikon E-800 Microscope and a computer-assisted image analysis system (Stereoinvestigator Software, MicroBrightField). The following counting parameters and settings were used: counting frame, 50 × 50 μm; grid size, 10 sites per section (60 × 100 μm); section evaluation interval, 5 after randomized start; magnification, 100-fold. Coefficient errors were calculated according to the study by Gundersen and Jensen (1987), and values ≤0.1 were accepted. The stereological experimenter was blinded to treatment assignment. Correct striatal injection was verified in each brain in vibratome-cut, coronal striatal tissue sections (40 μm, fixed overnight in 4% PFA in PBS) and was immunostained as described above.

Isradipine treatment and plasma concentration measurement

ISR (catalog #I6658, Sigma-Aldrich) exposure started 1 week before 6-OHDA lesioning. ISR was delivered by implantation of extended-release pellets (6 or 9 mg/kg/d; 42 d; Innovative Research of America) or subcutaneous osmotic minipumps (3 mg/kg/d; model 2004, Alzet). Pumps were loaded with ISR dissolved in vehicle [dimethylsulfoxide (DMSO)/PEG300]. Neuroprotective effects of ISR were assessed only in mice in which plasma concentrations of ISR >3 ng/ml were reached that correspond to human therapeutic steady-state plasma levels [Christensen et al., 2000; Park et al., 2009; Wang et al., 2013; SPC Lomir (compendium.ch/mpro/mnr/2604/html/)]. ISR mouse plasma concentrations were measured by liquid chromatography-tandem mass spectrometry. Diazepam was used as the in-

the generation of stable cell lines; Christina Pötschke for performing the retrograde tracing experiments; and Helmut Wratil, Jennifer Müller, Gospova Stojanovic, Bettina Tschugg, and Maximilian Pittl for expert technical assistance.

T.C. and H.J.D. are employees of Boehringer Inhelheim Pharma GmbH & Co KG. The authors declare no other competing financial interests.

Correspondence should be addressed to Jörg Striessnig, Institute of Pharmacy, Department of Pharmacology and Toxicology, Center for Molecular Biosciences, University of Innsbruck, Innrain 80-82/III, 6020 Innsbruck, Austria. E-mail: joerg.striessnig@uibk.ac.at.

DOI:10.1523/JNEUROSCI.2946-16.2017

 0270-6474/17/376762-17$15.00/0

ternal standard. Concentrations were calculated by comparing ISR/diazepam peak area ratios to those of a standard curve prepared in blank plasma. The serum ISR calibration curve was linear for ISR concentrations from 0.5 (detection level) to 250 ng/ml.

Retrograde tracing for UV laser microdissection

Retrograde tracing was performed as described previously (Liss et al., 2005; Krabbe et al., 2015). Briefly, rhodamine-coupled latex retrobeads (Lumafluor) were injected stereotactically into the dorsal striatum of adult mice. The stereotactic coordinates for unilateral tracing were according to distance from bregma (at bregma = 0.0 mm: coordinate 1: x = 1.9 mm, y = 0.98 mm, z = −3.2 mm; coordinate 2: x = 2.7 mm; y = −0.1 mm, z = −3.2 mm). At both coordinates, 100 nl of diluted retrobeads [1:1 in sterile artificial CSF (ACSF) solution] was injected with a speed of 50 nl/min. Mice were killed 7 d after the tracing procedure. For verification of striatal injection sites, brain tissue blocks containing the striatum were fixed overnight in 4% PFA in PBS and cut in coronal 60 μm sections using a vibratome (catalog #VT 1000S, Leica). Free-floating sections were processed as described previously (Liss et al., 2005; Krabbe et al., 2015) using rabbit anti-TH (1:1000 dilution; catalog #657012, Merck Millipore) as primary antibody and Alexa Fluor 488 goat anti-rabbit (catalog #A11034; Thermo Fisher Scientific) as secondary antibody. For structural visualization, sections were counterstained with Neuro Trace 640/660 deep-red Nissl staining solution (1:1000 in PBS; catalog #N21483, Thermo Fisher Scientific) for 10 min in the dark. Sections were analyzed using a Leica LMD7000 system, equipped with a halogen light source, a DFC360FX camera, and respective fluorescence filters. Images were captured with the LAS-AF6000 software (version 2.6.0.7266; Leica Microsystems).

UV laser microdissection and qRT-PCR analysis

UV laser microdissection (UV-LMD) of SN DA neurons from mouse brain sections (LMD7000 system, Leica Microsystems), cell lysis, cDNA synthesis, purification, multiplex nested PCR (for marker-gene analysis) and qRT-PCR of UV-LMD samples were performed as described previously (Gründemann et al., 2011; Poetschke et al., 2015). Only cDNA samples expressing the typical, multiplex-nested PCR-derived SN DA neuron marker profile [positive for TH and negative for calbindin d28k, CBd28k, L-glutatmate decarboxylase GAD65/67, and glial fibrillary acidic protein (GFAP)] were further analyzed by qRT-PCR.

Mouse TaqMan qRT-PCR assays with exon-spanning primers were acquired from Thermo Fisher Scientific and were labeled with 6-carboxyfluorescein as a reporter and with a nonfluorescent quencher, as follows: $mCa_v1.2$, Mm01188822_m1; $mCa_v1.3$ generic, Mm00551392_m1; $mCa_v1.3_L$, Mm01209927_g1; $mCa_v1.3_{43S}$: custom-made forward, CAG AAG ACT CCA AAC CAG AAG AAGA; reverse, TGG AAT TAT GGT TAT GAT GGT TAT GAC ACC; probe, FAM-TCAAACAGGAAATTCG–NFQ; $Ca_v1.3_{42A}$: forward, GGA AGT ACC CTG CGA AGA ACAC; reverse, CTC AGG CAG AGA ACT CTA AAG CAT; and probe, FAM-TTG CCC TAC AGA TGC TTG-NFQ. Information on multiplex-nested primers are given by Poetschke et al. (2015, their S2, Supplementary Table A). For absolute quantification of LTCC cDNA molecule numbers, defined amounts of DNA molecules were used for standard curve generation as previously described (Liss et al., 2001). Fragments of DNAs that covered the respective TaqMan assay locations were amplified using the following primers: $mCa_v1.2$: forward, TCACCACTCTGCTGCAGTTC; reverse, GACGAAACCCACGAAGATGT (amplicon size, 392 bp); $mCa_v1.3$generic: forward, TCGGGACTGGTCTATTCTGG; reverse, TACTTCCCCACCAGTCCTTG (amplicon size, 480 bp); $mCa_v1.3_L$: forward, ATCCCTACACCGAAGCTCCT; reverse, TCTCATCTGCCAGGTCCTCT (amplicon size, 413 bp); $mCa_v1.3_{43S}$: forward, CAAGGACTGGTGGGGAAGTA; reverse, CGATCATGCTTGCAGGAGTA (amplicon size, 500 bp); $mCa_v1.3_{42A}$: forward, TCCGAGCTGTGATCAAGAAA; reverse, AAATAAGCCCGAGTGGGAGT (amplicon size, 320 bp); PCR products were purified (QIAquick Gel Extraction Kit), quantified using a Qubit 3.0 Fluorometer (Thermo Fisher Scientific), and 0.1–1,000,000 molecules (in 10-fold dilutions) each were used as templates for the respective qRT-PCRs for standard curve generation.

cDNA molecules per SN DA neurons were calculated according to the following:

$$\text{cDNA molecules/cell} = \frac{S^{\left\lfloor \frac{C_t - y_{\text{intercept}}}{\text{slope}} \right\rfloor}}{\text{No}_{\text{cells}} * \text{cDNA fraction}}, \quad (1)$$

where S is serial dilution factor (i.e., 10); slope is the slope of the standard curve; $y_{\text{intercept}}$ is the y-intercept from absolute standard curve, reflecting one DNA molecule; No_{cells} is the number of harvested neurons per UV-LMD sample (i.e., 10), and cDNA fraction is the fraction of the UV-LMD cDNA reaction sample used as template in the qRT-PCR (i.e., 5 of 17).

Combined Ca^{2+} imaging and electrophysiology from SN DA neurons in adult mouse brain slices

Brain slices. Adult male C57BL/6 mice (12–15 weeks old) were anesthetized with isoflurane (B506; AbbVie Deutschland GmbH & 421 Co KG, Ludwigshafen, Germany) and subsequently decapitated without prior perfusion. The brain was rapidly removed and a block of tissue containing the mesencephalon was immediately cut out. Coronal slices (250–300 μm) containing the SN were cut with a vibration microtome (HM-650 V, Thermo Scientific) under cold (4°C), carbogenated (95% O_2 and 5% CO_2), glycerol-based modified ACSF (GACSF; Ye et al., 2006) to enhance the viability of neurons. GACSF contained the following (in mM): 250 glycerol, 2.5 KCl, 2 $MgCl_2$, 2 $CaCl_2$, 1.2 NaH_2PO_4, 10 HEPES, 21 $NaHCO_3$, and 5 glucose, adjusted to pH 7.2 with NaOH, resulting in an osmolarity of ~310 mOsm. Brain slices were transferred into carbogenated extracellular saline (ACSF). ACSF contained the following (in mM): 125 NaCl, 2.5 KCl, 2 $MgCl_2$, 2 $CaCl_2$, 1.2 NaH_2PO_4, 21 $NaHCO_3$, 10 HEPES, and 5 glucose, adjusted to pH 7.2 with NaOH, resulting in an osmolarity of ~310 mOsm. Slices were kept in a 35°C "recovery bath" for 20 min and then stored at room temperature (~24°C) for at least 30 min before recording. For the recordings, slices were transferred to a Sylgard-coated (Dow Corning) recording chamber (~1.5 ml volume) and, unless mentioned otherwise, continuously superfused with carbogenated ACSF at a flow rate of ~2 ml/min. For Ca^{2+} imaging, 250 μM sulfinpyrazone (S9509, Sigma-Aldrich) was added to the ACSF. All recordings were performed at 32°C controlled by an in-line solution heater (model SH27B, Warner Instruments) operated by a temperature controller (model TC-324B; Warner Instruments). To reduce glutamatergic and GABAergic synaptic input to the recorded neurons, 10 μM CNQX (6-cyano-7-nitroquinoxaline-2,3-dione; catalog #C127, Sigma-Aldrich), 50 μM DL-AP5 (DL-2-amino-5-phosphonopentanoic acid; catalog #BN0086, BIOTREND), and 100 μM picrotoxin (PTX; catalog #P1675, Sigma-Aldrich) were added to the ACSF.

Perforated patch-clamp recordings. Neurons in the SN were visualized with a fixed-stage upright microscope (model BX51WI, Olympus) using a 20× water-immersion objective (0.95 numerical aperture; 2 mm working distance; XLUMPLFL, Olympus) with a 4× magnification changer (U-TVAC, Olympus), infrared differential interference contrast optics (Dodt and Zieglgänsberger, 1994), and fluorescence optics. Ventral tier SN DA neurons were identified by the size and location of their somata, by electrophysiological fingerprints, and by *post hoc* immunohistochemistry for TH (Lacey et al., 1989; Richards et al., 1997; Ungless et al., 2001). Biocytin–streptavidin labeling combined with TH immunohistochemistry was performed as previously described (Hess et al., 2013).

Electrodes with tip resistances between 3 and 5 MΩ were fashioned from borosilicate glass (inner diameter, 0.86 mm; outer diameter, 1.5 mm; catalog #GB150-8P, Science Products) with a vertical pipette puller (catalog #PP-830, Narishige). Recordings were performed with an EPC10 Patch-Clamp Amplifier (HEKA) controlled by PatchMaster software (version 2.32; HEKA). Data were sampled at 10 kHz and low-pass filtered at 2 kHz with a four-pole Bessel filter. Whole-cell capacitance was determined by using the capacitance compensation (C-slow) of the EPC10 amplifier. The calculated liquid junction potential between the intracellular and extracellular solutions was also compensated [14.6 mV for ACSF; calculated with Patcher's Power Tools plug-in (http://www.mpibpc.mpg.de/groups/neher/index.php?page=software) for IGOR Pro 6, WaveMetrics].

Perforated-patch recordings were performed using protocols modified from the studies by Horn and Marty (1988) and Akaike and Harata (1994). Recordings were performed with a pipette solution containing

1% biocytin and the following (in mM): 128 K-gluconate, 10 KCl, 10 HEPES, and 2 $MgCl_2$, and adjusted to pH 7.3 with KOH, resulting in an osmolarity of ~300 mOsm. The patch pipette was tip filled with internal solution and backfilled with freshly prepared amphotericin B (~200 μg/ml; catalog #A4888, Sigma-Aldrich) containing internal solution to achieve perforated patch recordings. Amphotericin B was dissolved in DMSO (catalog #D8418, Sigma-Aldrich) and added to the modified pipette solution shortly before use. Ionophore-containing solutions were stored on ice and replaced every 4 h as needed. After obtaining a GigaOhm seal, the perforation process was monitored by constantly measuring the access resistance (R_a). Experiments were started after R_a had reached steady state and the AP amplitude was stable (20–30 min). Membrane rupture with a change to the whole-cell configuration was indicated by abrupt changes in R_a and/or AP amplitude. Such experiments were rejected.

Fluorometric imaging measurements. The imaging setup consisted of an Imago/SensiCam CCD camera with a 640 × 480 chip (Till Photonics) and a Polychromator IV (Till Photonics) coupled via an optical fiber into the upright microscope. Fura-2 was excited at 340, 360, or 380 nm (410 nm dichroic mirror; catalog #DCLP410, CHROMA). Emitted fluorescence was detected through a 440 nm long-pass filter. Data were acquired as 80 × 60 frames using 8 × 8 on-chip binning. Images were recorded in analog-to-digital units (ADUs) and stored and analyzed as 12 bit grayscale images. Before establishing the perforated patch-clamp configuration, Fura-2 stain was loaded into the neurons by electroporation (1 V with 1 ms pulse duration at 65 Hz for 10–15 s). The loading pipette contained intracellular saline and 3.6 mM Fura-2 (pentapotassium salt; catalog #F1200, Life Technologies). Loading was monitored at 360 nm excitation to reach comparable loading states (210 ± 30 ADU; $n = 5$). To measure Ca^{2+} dynamics, pairs of frames excited with 340 and 380 nm were taken at 25 Hz. The mean ADU value within a region of interest (ROI) from the cell body was used. The ROI was adjusted for each cell. For "background subtraction" for the whole time series, an adjacent second ROI was chosen. Data were analyzed as F_{340}/F_{380} ratios and presented as normalized F_{340}/F_{380} ratios. Since AP-associated Ca^{2+} dynamics are strongly frequency dependent, for combined Ca^{2+} imaging AP frequencies of analyzed SN DA neurons were adjusted in control conditions and during ISR application to a similar value of ~1.5 Hz (mean ± SD, 1.48 ± 0.06 Hz; $n = 20$; five neurons, four time points in each neuron) by current clamp. Neurons in which it was not possible to adjust the AP frequency accordingly were omitted from analysis.

Pharmacology for combined Ca^{2+} imaging and electrophysiology. ISR (catalog #BG0371, BIOTREND) diluted in ACSF was bath applied at a flow rate of ~2 ml/min (~1.5 ml volume of the recording chamber). In control experiments, 30 nM quinpirole (catalog #Q102, Sigma-Aldrich) drastically reduced the AP frequency 1–2 min after drug arrival in the bath. Note that in contrast to our previous studies (Dragicevic et al., 2014; Poetschke et al., 2015) we used experimental conditions in which robust and reversible effects of DHP channel blockers on pacemaker activity of SN DA neurons in *in vitro* brain slices can be observed (Guzman et al., 2010; Drion et al., 2011; Schiemann et al., 2012). This allows indirect monitoring of LTCC activity, which contributes to pacemaking.

L-type Ca^{2+} channel constructs

The stable $hCa_v1.2$ cell line expressed the human full-length $Ca_v1.2$ α1 subunit ($hCa_v1.2_{77WT}$, exons 1b/8b/-9*/22/32/33; Soldatov et al., 1995). This splice variant contains the smooth muscle-specific/brain-specific alternative exon 1b (Biel et al., 1991; Snutch et al., 1991; Welling et al., 1997) and displays high DHP sensitivity due to the alternative exons 8b (Welling et al., 1997), in contrast to the less DHP-sensitive cardiac-like exon 8a (Lacinová et al., 2000) and exon 22 (Soldatov et al., 1995; Zühlke et al., 1998). Stably expressed C-terminal human long ($hCa_v1.3_L$) and short ($hCa_v1.3_S$) $Ca_v1.3$ constructs differed from those of $Ca_v1.3$ α1 subunit (GenBank accession number EU363339) by containing exons 8b, 11, 32, and 44 (exon 44 only in $hCa_v1.3_L$; $hCa_v1.3_S$ stops after exon 41).

Generation of stable cell lines and cell culture

HEK293 cells stably expressing human smooth muscle $hCa_v1.2$ or $hCa_v1.3_L$ or $hCa_v1.3_S$ α1-subunits were generated using the Flp-In T-Rex system (Invitrogen). Briefly, α1-subunit cDNA was cloned into the pTO HA strepIII C GW FRT (flippase recognition target) vector (containing an FRT site and a hygromycin resistance gene) and transfected together with a Flp recombinase-expressing vector (pOG44) into HEK293 host cells (also containing an FRT site). Host cells already expressed human β3 and α2δ1 subunits. The α1-subunit construct was then integrated into the genome in a Flp recombinase-dependent manner. Hygromycin B (50 μg/ml; catalog #CP12.2, CARL ROTH) was used to select for stable transfectants. Single positive cell clones were subsequently picked, cultured, and characterized. Cells were cultured in DMEM (catalog #D6546, Sigma-Aldrich) supplemented with 10% fetal bovine serum (catalog #10270-106, Invitrogen), 2 mM L-glutamine (catalog #25030-032, Invitrogen), 10 U/ml penicillin G (catalog #P3032, Sigma-Aldrich), and 10 U/ml streptomycin (catalog #S6501, Sigma-Aldrich), and were maintained at 37°C in a humidified incubator with 5% CO_2. Cells were grown and split when they reached ~80% of confluence using 0.05% trypsin for cell dissociation. Twenty-four hours after plating onto poly-L-lysine-precoated 35 mm culture dishes, the expression of α1-subunit was induced using 1 μg/ml doxycycline (catalog #D1822, Sigma-Aldrich), and cells were kept <5% CO_2 at 30°C. Cells were subjected to patch-clamp experiments 20–72 h after induction.

For maintenance of stable cell lines, selection agents for each subunit were applied [α1, 50 μg/ml hygromycin B; β3, 500 μg/ml geneticin (catalog #10131–027, Invitrogen); and α2δ1, 15 μg/ml blasticidin S (catalog #A11139–03, Invitrogen)]. The biophysical properties of all stable cell lines were subjected to a rigorous biophysical characterization revealing the typical properties as expected for the $hCa_v1.3_L$, $hCa_v1.3_S$, and $hCa_v1.2$ splice variants from published transient transfection experiments (Bock et al., 2011; Lieb et al., 2014; see also Fig. 3*B*). This included a more negative activation and inactivation range for $hCa_v1.3_S$ ($V_{0.5,act}$ shifted by −7.2 mV; $V_{0.5,inact}$ by −3.2 mV in 2 mM Ca^{2+}) compared with $hCa_v1.3_L$ and more positive voltage-dependent gating of $hCa_v1.2$ ($V_{0.5,act}$ shifted by +16.7 mV; $V_{0.5,inact}$ shifted by +12.2 mV vs $hCa_v1.3_L$); the inactivation time course during 5 s depolarizations to the voltage of maximal activation (V_{max}) of $hCa_v1.3_S$ was faster compared with $hCa_v1.3_L$ (Bock et al., 2011); stable $hCa_v1.2$ displayed a faster and more complete inactivation than $hCa_v1.3_L$ (Koschak et al., 2003); isradipine sensitivity of $Ca_v1.3$ Ba^{2+} currents in the stable cell lines measured using square pulse protocols (Huang et al., 2013) was not significantly different compared with transiently transfected $Ca_v1.3$ constructs (GenBank accession number EU363339; data not shown) and was slightly higher for $hCa_v1.2$ channels (data not shown), which is in agreement with previous studies with transiently expressed $Ca_v1.2$ (Koschak et al., 2001; Xu and Lipscombe, 2001). Together, our new stable cell lines exhibit similar biophysical and pharmacological properties compared with transiently transfected LTCC constructs.

Whole-cell patch-clamp recordings in HEK293 cells

For whole-cell patch-clamp recordings, electrodes with a resistance of 1.8–3.8 MΩ were pulled from glass capillaries (borosilicate glass; catalog #64-0792, Harvard Apparatus) using a micropipette puller (Sutter Instruments) and fire polished with an MF-830 Microforge (Narishige). The pipette internal solution contained the following (in mM): 135 CsCl, 10 Cs-EGTA, 1 $MgCl_2$, 10 HEPES, and 4 ATP-Na_2 adjusted to pH 7.4 with CsOH. The bath solution contained the following (in mM): 2 $CaCl_2$, 170 choline-Cl, 1 $MgCl_2$, and 10 HEPES, adjusted to pH 7.3 with CsOH. Cells were recorded in the whole-cell patch-clamp configuration using an Axopatch 200B Amplifier (Molecular Devices). Recordings were digitized (Digidata 1322A Digitizer, Molecular Devices) at 40 or 50 kHz, low-pass filtered at 1–5 kHz, and subsequently analyzed using pClamp 10.2 software (Molecular Devices). Currents were leak subtracted on-line using P/4 subtraction or off-line. Compensation was applied for 60–90% of the series resistance. For the characterization of the voltage dependence of the stable cell lines, currents of <200 or >3000 pA were excluded. All voltages were corrected for a liquid junction potential of −9 mV.

Current–voltage (*I–V*) relationships were obtained by applying a 20-ms-long square pulse to various test potentials starting from a holding potential (HP) of −89 mV. The resulting *I–V* curves were fitted to the following equation:

$$I = G_{max}(V - V_{rev})/(1 + \exp[-(V - V_{0.5})/k]), \quad (2)$$

where I is the peak current amplitude, G_{max} is the maximum conductance, V is the test potential, V_{rev} is the extrapolated reversal potential, $V_{0.5}$ is the half-maximal activation voltage, and k is the slope factor. The voltage dependence of Ca^{2+} conductance was fitted using the following Boltzmann relationship:

$$G = G_{max}/(1 + \exp[-(V - V_{0.5})/k]. \quad (3)$$

The voltage dependence of inactivation was assessed by application of 20 ms test pulses to V_{max} before and after holding cells at various conditioning test potentials for 5 s (30 s intersweep interval; HP, −89 mV). Inactivation was calculated as the ratio between the current amplitudes of the test pulses. Steady-state inactivation parameters were obtained by fitting the data to the modified Boltzmann equation, as follows:

$$G = (1 - G_{max})/(1 + \exp[(V - V_{0.5,inact})/k_{inact}] + G_{max}, \quad (4)$$

where $V_{0.5,inact}$ is the half-maximal inactivation voltage and k_{inact} is the inactivation slope factor. The amount of inactivation during a 5 s depolarizing pulse from an HP of −89 mV to the V_{max} was quantified by calculating the remaining current fraction after 100, 250, or 5000 ms.

aSM tone protocol. To mimic typical voltage changes in aSM cells (Davis and Hill, 1999), voltage was ramped from −57 to −25 mV and immediately back to −57 mV (32 mV/s) with a sweep interval of 8 s (HP, −57 mV).

SN DA pacemaker protocol. Spontaneous pacemaker activity was recorded in whole-cell configuration at 36°C from an identified TH^+ SN DA neuron in a mouse brain slice (male; age, P12), and 276 single APs were averaged to create the SN DA AP command voltage, which was looped to mimic regular pacemaking (2.5 Hz). For all three channel constructs, >50% of Ca^{2+} current (I_{Ca}) was inactivated during SN DA pacemaking and was recovered during electrical inactivity at more hyperpolarized voltages.

Computational modeling of SN DA neuron-like defined command voltages

For simulation of SN DA burst activity patterns, voltage commands were modeled using the NEURON simulation environment (http://www.neuron.yale.edu/neuron; Hines and Carnevale, 1997). Computer-modeled voltage commands included oscillatory activity before and after the burst. I_{Ca} responses to the computer-modeled oscillatory activity closely resembled those obtained with the SN DA pacemaker command voltage recorded in slices. An SN DA neuron was constructed, similar to that described previously (Dougalis et al., 2017), as a single-compartment sphere 30 μm in diameter (total surface area, 2830 μm^2) having a total capacitance of 28 pF (assuming a specific membrane capacitance of 1 $\mu F/cm^2$) and an input resistance of 200 MΩ. The modeled neuron displayed spontaneous rodent SN DA neuron pacemaker-like APs at a frequency of ~2.5 Hz, using a linear unspecific leak conductance and the following nine Hodgkin–Huxley-like conductances: a transient Na^+ conductance (Komendantov et al., 2004); a delayed rectifier K^+ conductance (Komendantov et al., 2004); an A-type K^+-channel conductance (K_v4.3/KChip3; Liss et al., 2001); a hyperpolarization-activated unspecific cation conductance (HCN channel; unpublished data); a Ca^{2+}-activated K^+ conductance (Drion et al., 2011); and voltage-gated Ca^{2+} conductances reflecting L-, N-, and R-type Ca^{2+} channels (Amini et al., 1999) and T-type Ca^{2+} channels (Cav3.1; Poetschke et al., 2015). An outward Ca^{2+} pump and mechanisms of Ca^{2+} accumulation were included according to the study by Amini et al. (1999). For the modeling of SN DA neuron burst activity, a NMDA receptor-like conductance was added, which was derived from first-order kinetics of transmitter binding (Destexhe et al., 1994). Parameters were standardized to elicit three spike bursts with an intraburst frequency of ~14 Hz, followed by a (variable) pause of ~1500 ms. Modeled burst activity resembled typical *in vivo* recorded burst characteristics of rodent SN DA neurons, such as progressively decreasing spike amplitude, and increasing AP width and interspike interval (ISI; Grace and Bunney, 1984b). All conductances were described for their steady-state activation (A)/inactivation (B) gating mechanisms by first-order generalized Boltzmann functions. The rates of activation (τA)/inactivation (τB) were described by first-order generalized Boltzmann or Gaussian equations, as appropriate.

Drug perfusion

Cells were perfused by an air pressure-driven perfusion system (BPS-8 Valve Control System, ALA Scientific Instruments) with bath solution, in the presence or absence of ISR, with a flow rate of 0.5 ml/min. Each cell received a single concentration of ISR followed by 3 μM ISR to achieve full LTCC block (see Results section). Each day before measuring different ISR concentrations, control recordings with vehicle only were performed, using the same tubes subsequently used for ISR experiments. Complete exchange of the solution around the cell was achieved in <50 ms. All experiments were performed at room temperature (~22°C). ISR stock solutions were prepared in DMSO (maximum final DMSO concentration in experiments, 0.1% v/v).

Experimental design and statistical analysis

For all animal experiments, male mice were used at the ages indicated in the text. $Ca_v1.3^{-/-}$ mice were described in the study by Platzer et al. (2000; RRID:MGI:2181788). Data analysis was performed using Clampfit 10.2 (Axon Instruments), Igor Pro 6 (WaveMetrics), Spike2 (CED), SigmaPlot 12.5 (Systat Software), GraphPad Prism 5 (GraphPad Software), and SDS software 2.4 (Applied Biosystems). Unless stated otherwise, all values are presented as the mean ± SEM, mean ± SD, or mean and 95% confidence interval (CI) for the number of experiments (n) indicated in the text, in the figure legends or in the figures. Data were analyzed by unpaired or paired Student's t test, Mann—Whitney U test, one-way ANOVA with Bonferroni *post hoc* test, Kruskal–Wallis with Dunn's multiple-comparison *post hoc* test, as appropriate and indicated for individual experiments. Statistical significance was set at $p < 0.05$.

Results

No evidence for neuroprotection in $Ca_v1.3^{-/-}$ mice or by ISR pretreatment in a 6-OHDA PD mouse model

To investigate the neuroprotective potential of either systemic ISR administration or $Ca_v1.3$ deficiency (Platzer et al., 2000), SN DA neurons in mice were challenged with a striatal unilateral injection of 6-OHDA (Ilijic et al., 2011). Stereological analysis of TH^+ SN DA neurons 28 d after lesioning with 4.1 μg of 6-OHDA resulted in ~50% SN DA neuron loss (Fig. 1*A–D*) but revealed no relevant neuroprotection in mice lacking $Ca_v1.3$ channels (wild-type, $n = 23$; $Ca_v1.3^{-/-}$, $n = 27$; four independent experiments; Fig. 1*A*,*C*). Instead, a significant 14% decrease in the absolute number of SN neurons was found in the nonlesioned side of $Ca_v1.3^{-/-}$ mice compared with wild-type mice (Fig. 1*F*, statistics). Since germline deletion of $Ca_v1.3$ may lead to compensatory changes in Ca^{2+} channel expression during development, masking a role of $Ca_v1.3$ channels (Poetschke et al., 2015), we next tested whether pharmacological LTCC inhibition by ISR can protect wild-type SN DA neurons from 6-OHDA neurotoxicity. One week before 6-OHDA lesioning, ISR was applied via extended-release pellets (6 or 9 mg/kg/d) or subcutaneous Alzet osmotic mini-pumps (3 mg/kg/d), and only animals with ISR plasma concentrations therapeutically relevant in humans (≥3 ng/ml, 8.1 nM, after 5 weeks; Fig. 1*E*) were used for analysis. Again, 6-OHDA induced an ~50% TH^+ SN DA neuron loss, which ISR administration failed to rescue as neuronal counts were comparable to those in placebo-treated mice (ISR, $n = 18$; placebo, $n = 28$; four independent experiments; Fig. 1*B*,*D*). Together, neither the knockout of $Ca_v1.3$ nor treatment with ISR at therapeutically relevant plasma concentrations in mice enhanced the survival of SN DA neurons in the 6-OHDA PD model.

Distinct *in vitro* I_{Ca} properties of $Ca_v1.2$ and $Ca_v1.3$ isoforms during SN DA neuron-like pacemaker activity

To investigate whether a lower sensitivity of SN DA neuron LTCCs to ISR could contribute to the absence of its neuroprotec-

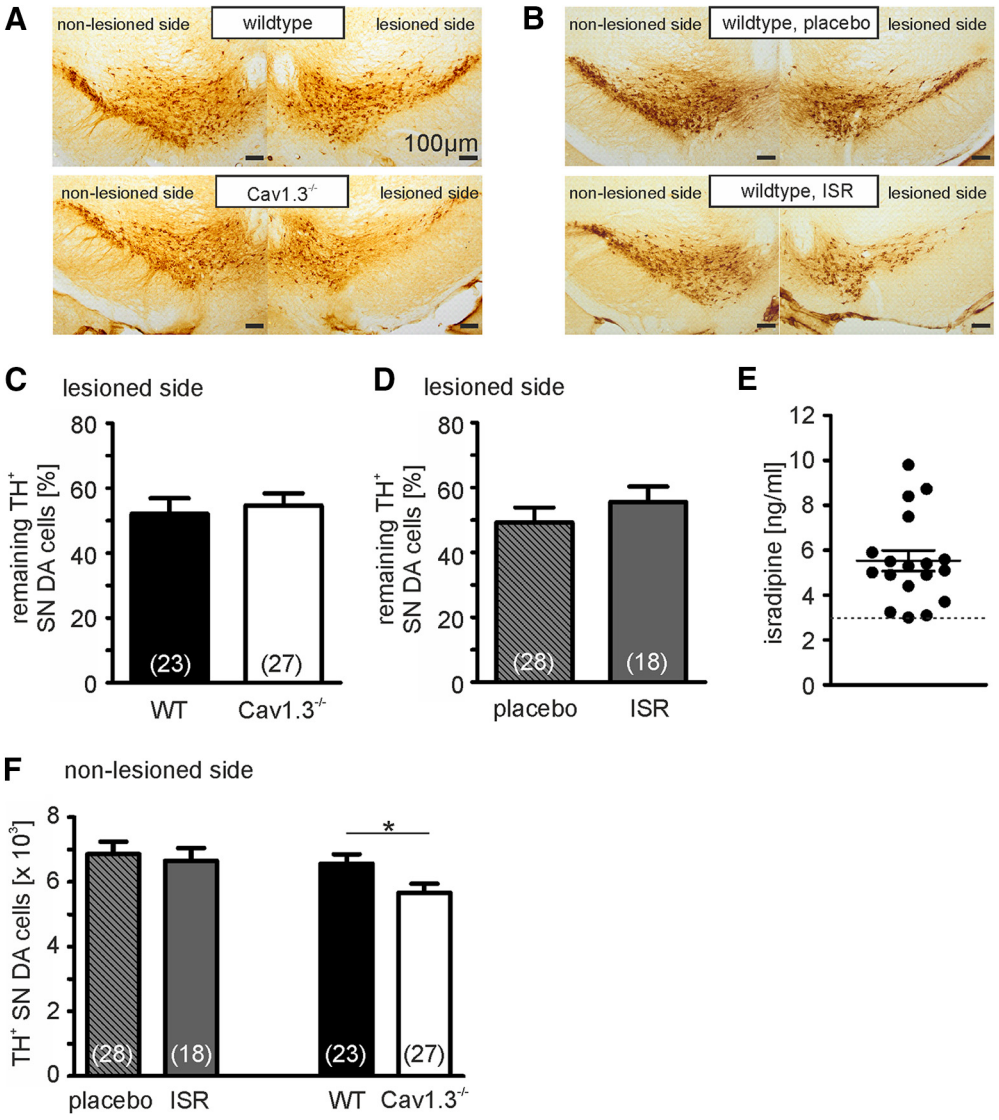

Figure 1. Evaluation of neuroprotective effects by $Ca_v1.3$ knockout or *in vivo* ISR pretreatment in a 6-OHDA PD mouse model (using male mice). ***A***, ***B***, Immunohistochemical stainings of TH^+ SN DA neurons in rostral sections of wild-type and $Ca_v1.3^{-/-}$ mice (***A***) or wild-type mice (***B***) treated with ISR (6 or 9 mg/kg) or placebo 7 d before unilateral injection with 4.1 μg of 6-OHDA. Scale bars, 100 μm. ***C***, ***D***, The percentage of neurons remaining in the injected side compared with the noninjected side for each mouse were calculated 28 d after lesioning. Data are reported as the mean ± SEM. ***E***, Distribution of ISR plasma levels in mice 35 d after pellet implantation with ISR plasma concentrations ≥3 ng/ml (mean ± SEM: 5.5 ± 0.5 ng/ml). ***F***, A statistically significant difference for the absolute numbers of TH^+ cells in the nonlesioned side was only observed between wild-type (WT) and $Ca_v1.3^{-/-}$ mice (wild-type mice: 6572 ± 285, $n = 23$; $Ca_v1.3^{-/-}$ mice: 5668 ± 282, $n = 27$; four independent experiments; $p = 0.03$; unpaired Student's *t* test) but not between ISR- or placebo-treated wild-type mice (ISR: 6655 ± 398, $n = 18$; placebo: 6861 ± 381, $n = 29$; four independent experiments). ***$p < 0.001$; **$p < 0.01$; *$p < 0.05$.

tive properties, we quantified *in vitro* LTCC ISR sensitivity during SN DA-like activity. Since $Ca_v1.2$ and $Ca_v1.3$ LTCCs in SN neurons comprise only a fraction of total I_{Ca} and are not accessible for isoform-specific pharmacological analysis (Philippart et al., 2016), we performed whole-cell patch-clamp recordings on HEK293 cells expressing $Ca_v1.2$ and $Ca_v1.3$ channels at near physiological conditions. Conditions included using physiological Ca^{2+} concentration (2 mM) as the charge carrier, using command voltages previously recorded from SN DA neurons, and measuring drug sensitivity under simulated steady-state tonic pacemaking. Low Ca^{2+} levels and depolarized voltages of SN APs required the generation of new stable cell lines expressing human $Ca_v1.2$ ($hCa_v1.2$) or human $Ca_v1.3$ ($hCa_v1.3$) variants that could reproducibly conduct large currents (<1000 pA) and allow reliable pharmacological analysis even when a large fraction of current is inactivated. C-terminally long $hCa_v1.3$ ($hCa_v1.3_L$) and short $Ca_v1.3$ ($hCa_v1.3_S$) splice variants are functionally and pharmacologically distinct (Bock et al., 2011; Huang et al., 2013, for review, see Striessnig et al., 2015; Zamponi et al., 2015). We therefore investigated whether both variants are expressed in individual laser-dissected mouse SN DA neurons using qRT-PCR (Fig. 2). Together with $Ca_v1.2$, we also detected robust expression of $Ca_v1.3$. $Ca_v1.3_L$ was the predominantly expressed splice variant, but the most abundant short splice variants in the brain, $Ca_v1.3_{43S}$ and $Ca_v1.3_{42A}$ (Bock et al., 2011; Tan et al., 2011), were also expressed in SN DA neurons (Fig. 2*C*). We also detected reduced mRNA levels for $Ca_v1.2$ and $Ca_v1.3$ with postnatal maturation, which is in line with previously described reduced LTCC currents in these neurons (Branch et al., 2014). Thus, stable cell lines expressing $hCa_v1.3_L$ and $hCa_v1.3_S$ (corresponding to $Ca_v1.3_{42A}$) were generated, and their extensive biophysical and pharmacological analysis demonstrated the expected LTCC cur-

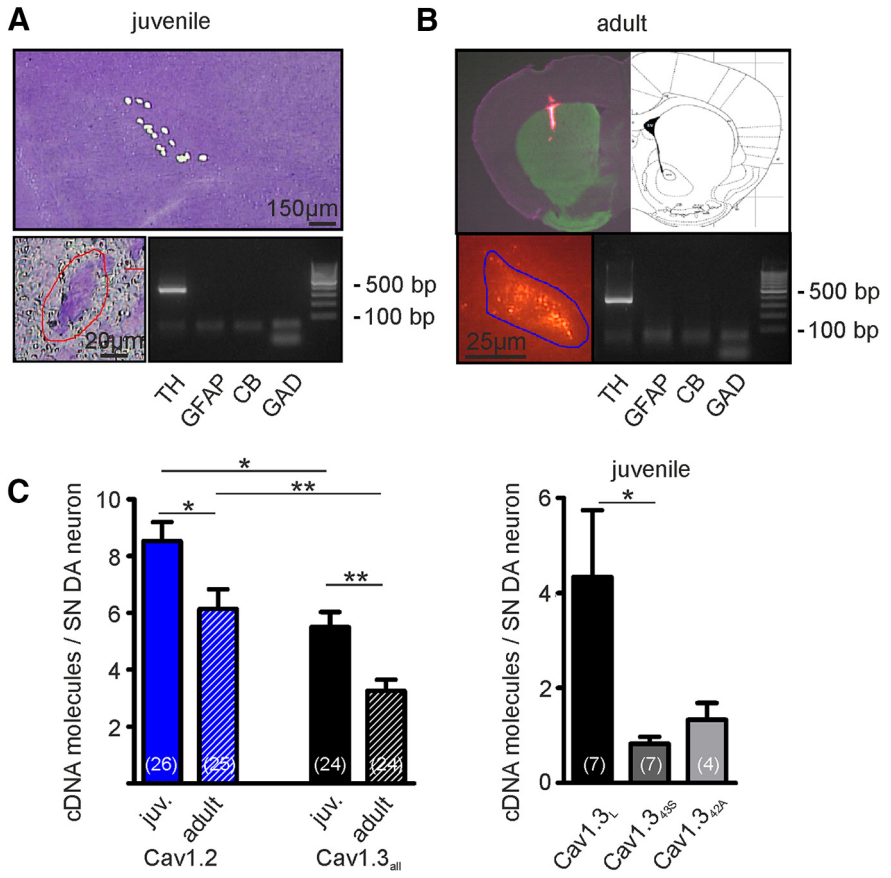

Figure 2. cDNA molecule number of $Ca_v1.2$ and $Ca_v1.3$ splice variants in individual laser-microdissected (LMD) SN DA neurons from juvenile and adult mice. ***A***, Overview of coronal midbrain section of a juvenile mouse stained with cresyl violet after UV-LMD of 10 SN DA neurons. Bottom left, Image of a single SN DA neuron before UV-LMD. Bottom right, Gel electrophoresis of marker gene RT-PCR products using ~30% of the cDNA as template. Note that only cDNA pools displaying the marker gene profile for SN DA neurons without contaminations (TH^+; $GFAP^-$, $CBd28k^-$, and $GAD65/67^-$) were further analyzed by qRT-PCR. ***B***, Verification of the striatal injection site of retrograde tracer (pink signal) for an adult mouse in a coronal TH-counterstained (green) and Nissl-counterstained (violet) section, aligned with the respective panel from the mouse brain atlas (Paxinos and Franklin, 2001). Bottom left, Image of a retrogradely traced adult mouse SN DA neuron before UV-LMD. Bottom right, Agarose gel electrophoresis of marker gene RT-PCR. ***C***, Mean numbers of cDNA molecules of LTCC α1-subunits in single mouse SN DA neurons. Left, Comparison of $Ca_v1.2$ and $Ca_v1.3$ (all splice variants) expression in SN DA neurons from juvenile (P13) and adult (P90) mice. Right, Comparison of expression levels of major brain $Ca_v1.3$ splice variants in juvenile SN DA neurons. $Ca_v1.3_{all}$: assay detects all $Ca_v1.3$ splice variants; $Ca_v1.3_L$: assay specific for long $Ca_v1.3_L$; $Ca_v1.3_{43S}$ and $Ca_v1.3_{42A}$: assay detects the short $Ca_v1.3$ splice variants only (Bock et al., 2011; Huang et al., 2013). $Ca_v1.3_{42A}$ corresponds to the short $Ca_v1.3$ construct used to generate the $hCa_v1.3_S$ stable cell line. Data are given as numbers of cDNA molecules/SN DA neuron determined via absolute DNA standard curves generated from dilution series of defined numbers of the respective PCR amplified and quantified target DNA molecules. Data are reported as the mean ± SEM (numbers of analyzed cDNA pools given in bars). Statistical significance was determined using the Mann–Whitney *U* test (***C***, left) or Kruskal–Wallis test (***C***, right; $p = 0.0246$) with Dunn's Multiple Comparison *post hoc* test. Outliers were identified using Grubbs' outlier test and excluded from analysis. ***$p < 0.001$; **$p < 0.01$; *$p < 0.05$.

rent properties (for details, see Materials and Methods; Fig. 3*A*,*B*; Table 1).

In vivo SN DA neurons exhibit the following three main firing modes: intrinsically generated regular pacemaker activity with a low frequency (~2.5 Hz) and synaptically driven/facilitated irregular single spike or burst activity (Grace and Bunney, 1984a,b). To investigate LTCC I_{Ca} characteristics during intrinsic pacemaker activity of SN DA neurons, we recorded APs in mouse brain slices (mean frequency, 2.5 Hz; for details, see Materials and Methods; Fig. 3*C*) and used their profiles as command voltages. Protocols were started from an HP of −89 mV, where LTCCs are fully available for activation (Fig. 3*A*). During pacemaking, I_{Ca} decreased due to the more depolarized voltages of the SN DA APs (Fig. 3*C*,*D*, typical I_{Ca} waveforms) with different time courses for each of the three LTCC constructs (Fig. 3*D*–*F*). Inactivation curves were best fitted by a double-exponential decay (Fig. 3*F*, time constants and statistics). Steady-state availability of LTCCs during 2.5 Hz pacemaking was similar for all three channels (16.1 ± 1.3%, 15.2 ± 1.7%, or 23.6 ± 4.0%, respectively, for $hCa_v1.3_S$, $hCa_v1.3_L$, or $hCa_v1.2$; Fig. 3*F*). Current inactivation was composed of a voltage- and Ca^{2+}-dependent process, since it was slower with Ba^{2+} as the charge carrier (data not shown). All three LTCCs conducted I_{Ca} during the repolarization after the AP spike [i.e., the AP spike-mediated I_{Ca} (I_{AP}); Fig. 3*D*]. However, due to their more negative operation range, only the $hCa_v1.3$ splice variants conducted I_{Ca} during the slow-depolarizing phase preceding AP spikes [I_{Ca} during ISI (I_{ISI}); Fig. 3*A*], which contributed a large fraction of the total Ca^{2+} charge. Integrated I_{ISI} measured during the first AP, initiating a train of spikes, was significantly greater compared with integrated I_{AP} of the same AP, and this proportion was significantly greater for $hCa_v1.3_S$ (3.4 ± 0.3-fold; $n = 35$) than for $hCa_v1.3_L$ (1.8 ± 0.1-fold; $n = 16$; $p = 0.0001$, unpaired Student's *t* test). Strikingly, this higher contribution of I_{ISI} to total integrated current was maintained when ~70% of $hCa_v1.3$ LTCCs were inactivated (not illustrated). Our data demonstrate that during SN DA-like intrinsic pacemaker activity, only a small fraction of LTCCs is active at steady state. Moreover, only $Ca_v1.3$ channels carry a substantial fraction of total I_{Ca} at subthreshold potentials between spikes during typical SN DA neuron pacemaker activity.

Isoform- and splice variant-dependent *in vitro* ISR sensitivity during SN DA neuron-like pacemaker activity

To quantify the ISR sensitivity of LTCCs during SN DA-like pacemaker activity, we measured the concentration-dependent inhibition of steady-state I_{Ca} during SN DA pacemaking command potentials. After steady-state equilibrium was reached, 1–50 nM ISR was applied, followed by complete LTCC block with 3 µM ISR (Fig. 4*A*,*B*) to allow for the quantification of a remaining ISR-insensitive component (including gating currents; Fig. 4, see legend) for off-line subtraction (Fig. 4*A*). Inhibition by ISR was also corrected for a slow linear current decay observed in control cells perfused with only the vehicle (Fig. 4*C*, insets). Both I_{ISI} and I_{AP} were inhibited similarly by ISR, but, due to the greater amplitude, analysis was performed on I_{AP}. $Ca_v1.3$ ISR sensitivity during SN DA-like activity was splice variant specific [mean (95% CI): IC_{50} $hCa_v1.3_L$, 6.9 nM (5.8–8.3 nM); $hCa_v1.3_S$, 16.8 nM (14.1–19.9 nM)], with $hCa_v1.3_L$ displaying an approximately threefold higher sensitivity ($p < 0.0001$). $hCa_v1.2$ channels required significantly ($p < 0.0001$; 2.4- to 5.8-fold) lower doses for half-maximal inhibition (mean,

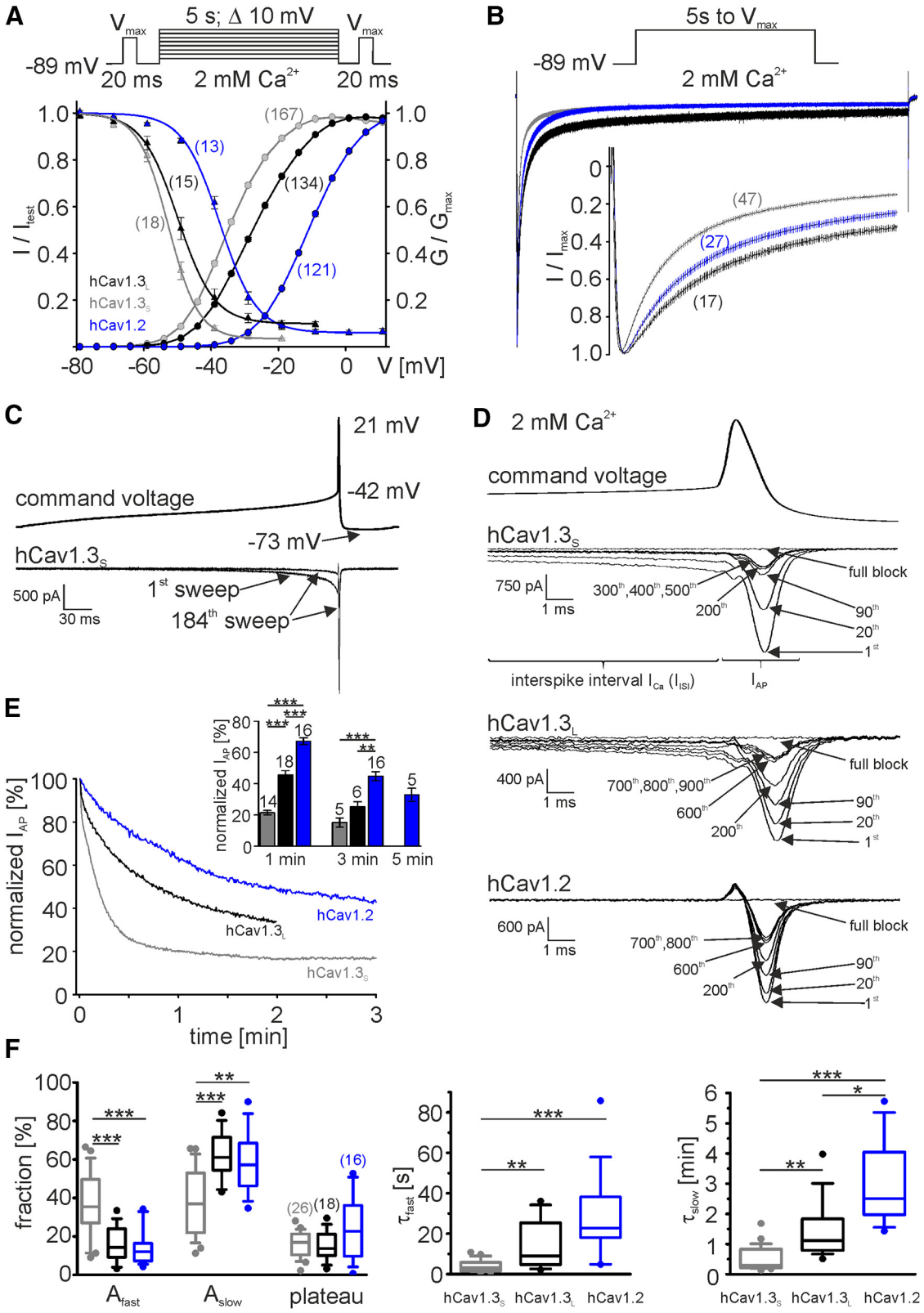

Figure 3. Biophysical properties of the newly generated stable cell lines and time-dependent decrease of LTCC I_{Ca} during simulated regular SN DA-like pacemaking (2.5 Hz; 2 mM Ca^{2+}). $hCa_v1.2$ (blue), $hCa_v1.3_S$ (gray), and $hCa_v1.3_L$ (black). ***A***, Voltage dependence of activation and inactivation; normalized steady-state activation (circles) and inactivation (triangles) curves were obtained as described in Materials and Methods. Currents <200 and >3000 pA were prospectively excluded from analysis. For statistics see Table 1. ***B***, Inactivation of stable cell lines during a 5-s-long depolarizing pulse from a holding potential of −89 mV to V_{max}. Insets show the first 150 ms. Vertical lines represent error bars (mean ± SEM). For statistics see Table 1. ***C***, AP waveform of an SN DA neuron used as command voltage to mimic regular pacemaking (top) and representative traces of the first (100%) and 184th (equilibrium) sweep of I_{Ca} through $hCa_v1.3_S$ (bottom). ***D***, Representative current traces of $hCa_v1.3_S$, $hCa_v1.3_L$, and $hCa_v1.2$ are shown (with components insensitive to 3 μM ISR subtracted; for details, see Fig. 4*A*). All three LTCC isoforms conduct I_{AP}. Only $Ca_v1.3$ channel constructs give rise to I_{ISI}. ***E***, Time course of I_{Ca} decay of representative recordings for each LTCC subtype. I_{AP} amplitude was normalized to the peak I_{AP} amplitude of the first SN DA AP after holding the cell at −89 mV. At the end of each recording, LTCC I_{Ca} was completely blocked by 3 μM ISR and remaining ISR-insensitive current components (*Figure legend continues.*)

Table 1. Biophysical properties of newly generated stable cell lines expressing $hCav1.3_L$, $hCav1.3_S$, or hCav1.2 together with human $\beta3$ and $\alpha2\delta1$ (2 mM Ca^{2+})

2 mM Ca^{2+}	$V_{0.5}$ (mV)	k (mV)	Act thresh (mV)	$V_{0.5,inact}$ (mV)	k_{inact} (mV)	Plateau (%)	r100 (%)	r250 (%)	r5000 (%)	*n*
Voltage dependence of activation										
$hCav1.3_L$	−27.7 ± 0.3	7.2 ± 0.1	−54.2 ± 0.3							134
$hCav1.3_S$	−34.9 ± 0.3***	6.0 ± 0.1***	−56.3 ± 0.3***							167
hCav1.2	−11.0 ± 0.2***,+++	6.9 ± 0.1***,+++	−36.3 ± 0.2***,+++							121
Voltage dependence of inactivation										
$hCav1.3_L$				−49.5 ± 1.2	4.8 ± 0.2	9.5 ± 1.2				15
$hCav1.3_S$				−52.7 ± 0.8*	4.1 ± 0.2*	3.7 ± 0.5***				18
hCav1.2				−37.3 ± 0.6***,+++	5.4 ± 0.2+++	5.6 ± 1.0*				13
5 s inactivation										
$hCav1.3_L$							35.6 ± 1.8	20.5 ± 1.5	6.1 ± 0.9	17
$hCav1.3_S$							17.0 ± 0.9***	9.3 ± 0.7***	2.7 ± 0.3***	47
hCav1.2							28.0 ± 1.7**,+++	14.3 ± 1.3*,++	3.1 ± 0.5*	27

All values are presented as the mean ± SEM for the indicated number of experiments (*n*). $V_{0.5}$, Half-maximal activation voltage; k, slope factor; act thresh, activation threshold; $V_{0.5,inact}$, half-maximal inactivation voltage; k_{inact}, inactivation slope factor. Parameters of voltage dependence of activation or inactivation were obtained as described in Methods and Materials. The *r* values represent the fraction of I_{Ca} remaining after 100, 250, or 5000 ms during a 5 s pulse to V_{max}. Statistical significance was determined using one-way ANOVA ($V_{0.5}$, k, act thresh, $V_{0.5,inact}$, plateau, r100: $p < 0.0001$) with Bonferroni's *post hoc* test or Kruskal–Wallis (k_{inact}; r250: $p < 0.0001$; r5000: $p = 0.0009$) with Dunn's multiple-comparison test. Statistical significances of *post hoc* tests are indicated for comparison vs $hCav1.3_L$ (*,**,***) and vs $hCav1.3_S$ ($^{+}$, $^{++}$, $^{+++}$): ***$p < 0.001$; **$p < 0.01$; *$p < 0.05$.

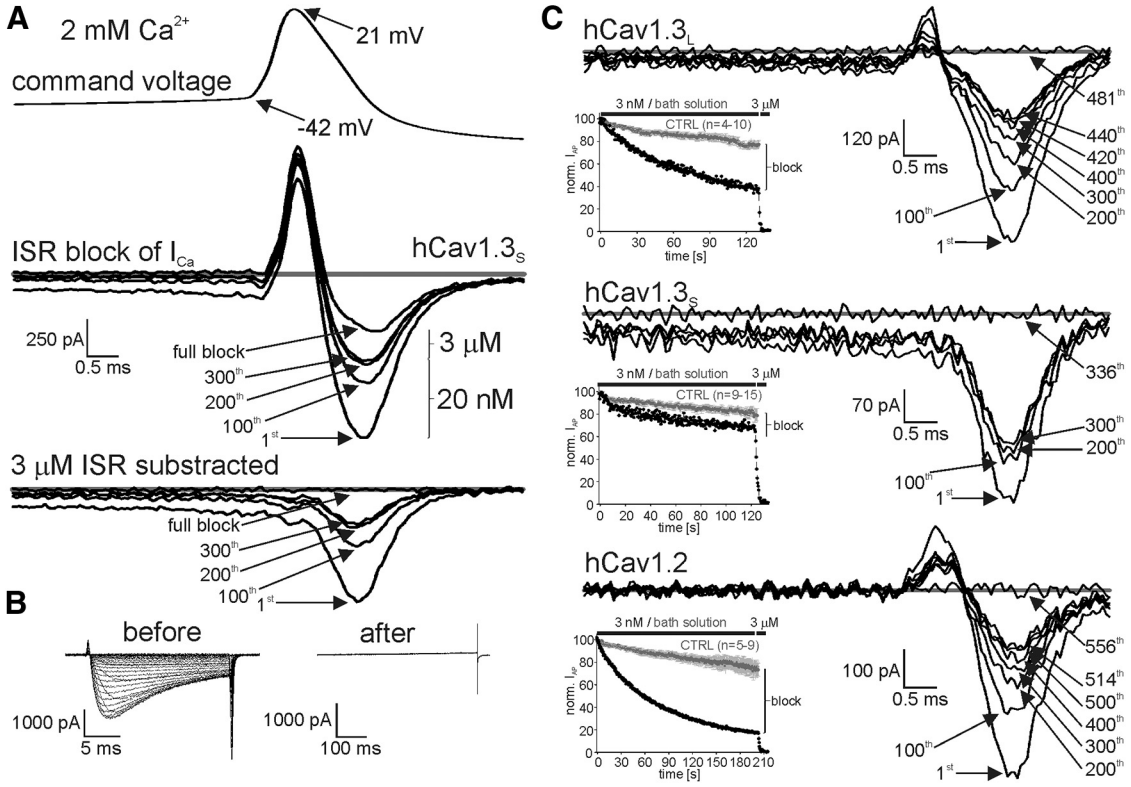

Figure 4. ISR sensitivity of LTCC steady-state I_{Ca} during simulated SN DA neuron pacemaking (2.5 Hz, 2 mM Ca^{2+}). ***A***, Example for the inhibition of I_{Ca} through $hCa_v1.3_S$ channels using 20 nM ISR. The cell was depolarized using the SN DA neuron pacemaking protocol and was perfused with bath solution only. After reaching steady-state I_{Ca} (Fig. 3), I_{Ca} was inhibited with 20 nM ISR followed by complete inhibition with 3 μM ISR to quantify the remaining ISR-insensitive current components. This was subtracted from traces to obtain pure LTCC-mediated I_{Ca} (***A***, bottom trace) and to quantify I_{AP} amplitudes. The outward current component occurring at the peak of the AP spike has also been shown in other publications (Patil et al., 1998; Helton et al., 2005; Marcantoni et al., 2010; Ortner et al., 2014) and was larger in recordings with large ON-gating currents (Q_{ON}). Its amplitude was slightly reduced after complete LTCC block by 3 μM ISR but persisted together with an ISR-insensitive inward component. Both components were also observed in nontransfected HEK293 cells, which did not conduct any Ca^{2+} currents. It may therefore be composed of Q_{ON} and a passive non-LTCC component. ***B***, Right, The complete LTCC inhibition by 3 μM ISR was confirmed by a subsequent ramp protocol (−89 to +71 mV, 500 ms). Left: The *I–V* of the example cell before ISR application is shown for comparison. ***C***, Representative experiments illustrating inhibition of I_{Ca} through $hCa_v1.3_L$, $hCa_v1.3_S$, or $hCa_v1.2$ using 3 nM ISR. Insets, Inhibition by ISR was corrected for linear current decay quantified during the perfusion of cells with bath solution only (CTRL shown in gray; mean ± SEM for all data points).

←

(*Figure legend continued.*) were subtracted off-line. The inset shows mean values ±SEM (and n-numbers) of each construct after 1, 3, and 5 min of pacemaking. ***F***, Curves were best described by a double-exponential function, and parameters are given as median (10th to 90th percentile; outliers illustrated as points). Statistical significance was determined using the Kruskal–Wallis test (A_{fast}, A_{slow}, τ_{fast}, τ_{slow}: $p < 0.0001$) with Dunn's multiple-comparison *post hoc* test. ***$p < 0.001$; **$p < 0.01$; *$p < 0.05$.

2.9 nM (95% CI, 2.2–3.9 nM); Figs. 4*C*, 5*B*) compared with the $Ca_v1.3$ variants. Together, these data demonstrate that with IC_{50} values in the low-nanomolar range, ISR sensitivity during continuous SN DA-like activity is much higher than previously reported for ISR and other potent DHP channel blockers using standard square pulse protocols (Koschak et al., 2001;

Xu and Lipscombe, 2001; Huang et al., 2013). Moreover, inhibition is isoform and splice variant dependent. As a consequence, the inhibition of $Ca_v1.3_S$ channels, which are robustly expressed in the SN (Bock et al., 2011) and in laser-dissected mouse SN DA neurons (Fig. 2), require almost six times higher ISR concentrations than $Ca_v1.2$.

ISR sensitivity of $hCa_v1.2$ during simulated arterial smooth muscle activity

The dose-limiting side effects of ISR (Parkinson Study Group, 2013) are due to excessive vasodilation and are thus determined by the inhibition of $Ca_v1.2$ channels in aSM (Moosmang et al., 2003; Zhang et al., 2007). Therefore, the sensitivity of $Ca_v1.2$ channels to inhibition by ISR in aSM versus the LTCCs in SN DA neurons is an important determinant for the therapeutic window of the drug for neuroprotection in the ongoing phase III trial (NCT02168842). Therefore, we compared the ISR sensitivity of $hCa_v1.2$ during simulated aSM electrical activity to the LTCC sensitivity during SN DA pacemaking. At physiological pressures, the resting membrane potential of aSM cells is in the range of −40 to −60 mV and increases with graded membrane depolarizations induced by transmural arterial pressure or longitudinal stretch (for review, see Davis and Hill, 1999). This drives a $Ca_v1.2$-mediated window current that triggers Ca^{2+}-dependent muscle contraction (Fleischmann et al., 1994; Moosmang et al., 2003). In our study, we mimicked aSM tone-induced depolarizations by applying depolarizing ramps (32 mV/s) from −57 to −25 mV and back to −25 mV separated by 6 s at −57 mV (Fig. 5*A*). This voltage range coincided with the window current range of $hCa_v1.2$ (Fig. 3*A*). When starting from an HP of −89 mV (all LTCCs available), this waveform induced a pronounced decrease in I_{Ca} amplitude, resulting in a steady-state equilibrium of only 2.7 ± 0.2% ($n = 40$) of the maximum I_{Ca} measured before by a short pulse to V_{max}. After this steady-state I_{Ca} was reached, 0.3–10 nM ISR was applied followed by a subsequent full block by 3 μM ISR (Fig. 5*A*). Control cells were perfused only with the vehicle to quantify the slow linear current rundown for the correction of ISR inhibition data (Fig. 5*A*, right) as for recordings using the SN DA-like command voltage. The resulting concentration–response relationship revealed a mean IC_{50} value of 1.5 nM (95% CI, 1.2–1.7 nM; Fig. 5*B*). These experiments demonstrate that $hCa_v1.2$ channels become more sensitive to ISR during aSM-like activity. This predicts a significant twofold lower IC_{50} value compared with SN DA-stimulated $hCa_v1.2$ and a 4.6-fold ($hCa_v1.3_L$) and 11.2-fold ($hCa_v1.3_S$) lower IC_{50} values compared with SN DA-stimulated $hCa_v1.3$ splice variants (Fig. 5*B*, statistics). Together, our *in vitro* data predict that at the given low-nanomolar concentrations, ISR blocks SN DA $Ca_v1.2$ and in particular $Ca_v1.3$ SN DA LTCCs to a significantly lesser extent than $Ca_v1.2$ channels in aSM.

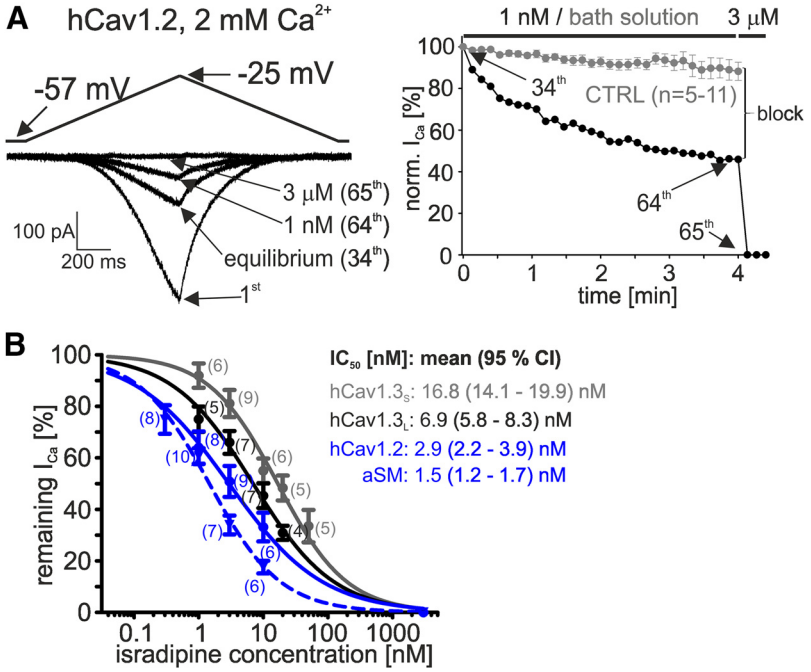

Figure 5. ISR sensitivity of $hCa_v1.2$ steady-state I_{Ca} during simulated aSM tone and ISR concentration–response curves for SN DA and aSM LTCCs (2 mM Ca^{2+}). $hCa_v1.2$ (blue; SN DA, solid line; aSM, dashed line), $hCa_v1.3_S$ (gray), and $hCa_v1.3_L$ (black) are shown. ***A***, aSM activity mimicked by voltage ramps. Starting from an HP of −89 mV, voltage was ramped from −57 to −25 mV and back to −57 mV at 32 mV/s and with an intersweep interval of 8 s at −57 mV. When I_{Ca} became stable ("equilibrium"), cells were perfused with vehicle (control, CTRL) or different concentrations of ISR and subsequently I_{Ca} was completely blocked by 3 μM ISR. Right, Normalized current of the same recording illustrating inhibition by 1 nM with time (1 pulse/8 s). Last sweep before drug application (34th sweep, "equilibrium," left) was set to 100% and the percentage of inhibition was calculated after subtracting current decay in control cells (gray; mean ± SEM) from ISR effects. ***B***, Concentration–response curves for LTCC steady-state I_{Ca} inhibition by ISR during simulated SN DA neuron pacemaking ($hCa_v1.3$, $hCa_v1.2$) and during aSM-like activity ($hCa_v1.2$). Data were fitted to a sigmoidal dose–response equation with variable slope (Hill slopes: $hCa_v1.3_S$, −0.81 ± 0.06; $hCa_v1.3_L$, −0.70 ± 0.06; $hCa_v1.2$, −0.60 ± 0.09; $hCa_v1.2$ aSM, −0.79 ± 0.06). Statistical significance was determined using the extra sum-of-squares *F* test (Hill slopes, $p = 0.797$; IC_{50} values, $p < 0.0001$). Significance level was set to $p < 0.05$.

Increased *in vitro* LTCC Ca^{2+} influx associated with SN DA neuron-like bursting activity

The finding that $Ca_v1.2$ and $Ca_v1.3$ LTCCs are largely inactivated during simulated oscillatory activity prompted us to study differences in Ca^{2+} entry through these channels during burst activity of SN DA neurons. Bursts in SN DA neurons consist of a small group of high-frequency spikes, followed by afterhyperpolarization (AHP)-induced pauses (Grace and Bunney, 1984b; Paladini and Roeper, 2014), which may allow LTCCs to partially recover from the pronounced steady-state inactivation imposed by preceding oscillatory activity. Notably, bursting has been associated with SN DA neuron vulnerability to degeneration and PD (Schiemann et al., 2012; Dragicevic et al., 2015). Here, we computer modeled a typical SN DA three spike burst intercepting oscillatory pacemaker activity (Grace and Bunney, 1984b), followed by a 1.5 s AHP per pause before oscillatory activity resumed (see Materials and Methods) and used it as a command protocol to address I_{Ca} during SN DA-like bursts. Oscillatory activity resulted in the expected pronounced I_{Ca} decay, and again only $hCa_v1.3$ constructs conducted I_{ISI} (Fig. 6*A*, right). When I_{Ca} became stable, the burst was elicited (Fig. 6*A*). For analysis, the integrated I_{Ca} during one AP (obtained as the mean of five APs) preceding the burst, was set to 100% and compared with I_{Ca} during the burst integrated over the time period equivalent to one AP. During the burst, integrated I_{Ca} of all three LTCC isoforms was significantly higher compared with the preceding APs at steady state (Fig. 6*B*, statistics). In contrast, total integrated I_{Ca} during APs following

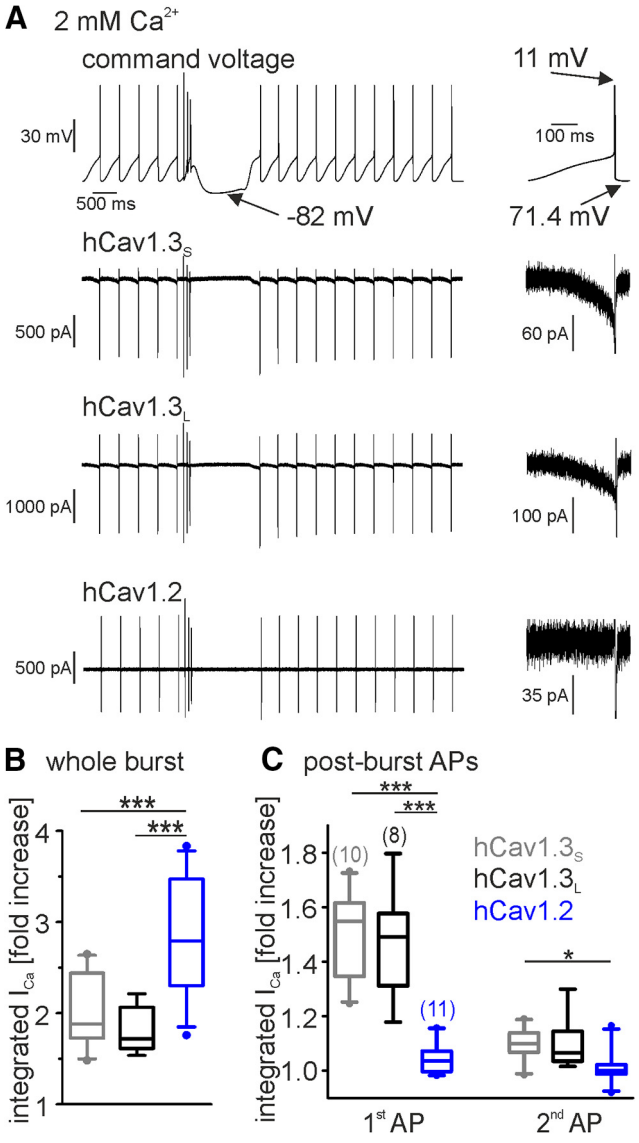

Figure 6. Integrated I_{Ca} during and after a simulated SN DA neuron three spike burst (2 mM Ca^{2+}) measured for $hCa_v1.2$ (blue), $hCa_v1.3_S$ (gray), and $hCa_v1.3_L$ (black). ***A***, Cells were stimulated using a modeled 2.4 Hz pacemaker protocol. After I_{Ca} stabilization, regular pacemaking was followed by a three spike burst followed by a 1.5-s-long AHP (maximum, −82 mV). The last five APs preceding the burst (baseline) are shown. Representative I_{Ca} traces are given for each construct. Right, One single AP command voltage and I_{ISI} responses for all three LTCCs (outward signal and I_{AP} were cutoff; again only the $Ca_v1.3$ constructs conducted I_{ISI}). ***B***, ***C***, The integrated I_{Ca} during a single AP (obtained as the mean of the five preceding APs) before the burst was set to 100% and compared with I_{Ca} during the three spike burst integrated over the time period equivalent to one AP (***B***) or the integrated I_{Ca} of the first or second AP after the AHP (***C***). Parameters are given as the median (10th to 90th percentile; outliers illustrated as points). The statistical significance between LTCC constructs was determined using one-way ANOVA (first AP, $p < 0.0001$; second AP, $p = 0.0189$; whole burst, $p < 0.0001$) with Bonferroni *post hoc* test: ***$p < 0.001$; **$p < 0.01$; *$p < 0.05$. Although the I_{AP} amplitude of the first and second postburst AP was increased for all three LTCC constructs (data not shown), total Ca^{2+} influx (integrated I_{Ca}) was only significantly increased for $Ca_v1.3$ constructs (first AP: $hCa_v1.3_S$, $p = 0.0006$; $hCa_v1.3_L$, $p = 0.0007$; second AP: $hCa_v1.3_S$, $p = 0.0020$; $hCa_v1.3_L$, $p = 0.0126$; paired Student's *t* test). Integrated I_{Ca} through all three LTCCs was significantly higher during the burst ($hCa_v1.3_S$, $p < 0.0001$; $hCa_v1.3_L$, $p = 0.0003$; $hCa_v1.2$, $p < 0.0001$; paired Student's *t* test).

the AHP was significantly increased to a similar degree for both $Ca_v1.3$ variants but not for $Ca_v1.2$ (Fig. 6*C*). These data predict that burst activity in SN DA neurons is associated with an increased Ca^{2+} influx mediated by LTCCs.

Our data, therefore, provide evidence that the subthreshold LTCCs contributing to the supralinear increase in dendritic Ca^{2+} signals during faster spiking of SN DA neurons is due to the activation of the $Ca_v1.3$ subtype (Hage and Khaliq, 2015), whereas the activation of both isoforms underlies this phenomenon during bursts (Hage and Khaliq, 2015). Therefore, their relative contribution to dendritic Ca^{2+} load may differ depending on the firing mode.

Effect of ISR on SN DA neuron *in vitro* pacemaker activity and related somatic Ca^{2+} transients

Our pharmacological data for ISR from stable cell lines, together with our 6-OHDA PD *in vivo* data, suggest that therapeutically relevant plasma levels are insufficient to block LTCCs in SN DA neurons and/or activity-related somatic Ca^{2+} oscillations. To test this, we performed combined perforated-patch current-clamp and ratiometric Fura-2 Ca^{2+} imaging experiments for SN DA neurons in adult mouse brain slice preparations. Depending on experimental conditions, ISR or other DHP channel blockers either decrease the precision of pacemaking without affecting its frequency in rodent SN DA neurons *in vitro*, which is evident as an increase in the coefficient of variation (CV) of the ISI (Drion et al., 2011; Branch et al., 2014; Dragicevic et al., 2014; Poetschke et al., 2015), or they reduce pacemaker precision as well as pacemaker frequency in a concentration-dependent manner with complete suppression of SN DA neuron activity at micromolar DHP concentrations (Nedergaard et al., 1993; Mercuri et al., 1994; Putzier et al., 2009; Branch et al., 2014; Sun et al., 2017). The cause for these differences of DHP channel blockers on SN DA neuron activity *in vitro* is still not clear (Costa, 2014), but they are most likely due to minor differences (<1%) in Na^+ conductance, caused by slightly different experimental conditions (Drion et al., 2011). We selected experimental conditions to maximize the possible effects of ISR on SN DA neuron activity. As evident in Figure 7, the exposure of adult neurons to ISR for 30 min had a concentration-dependent effect on pacemaking. During a 30 min exposure to 30 nM ISR, CV increased significantly without a change of mean frequency (Fig. 7*A*,*D*), whereas a 300 nM concentration not only significantly reduced pacemaker precision but also its frequency (Fig. 7*B*,*D*). ISR with a 3 μM concentration almost fully inhibited SN DA neuron activity (Fig. 7*C*,*D*). This effect was reversible upon washout, as shown for 300 nM ISR (Fig. 8*A*), excluding a nonspecific, time-dependent decrease in pacemaking.

These data are in agreement with our pharmacological data (Fig. 5*B*) showing only a partial inhibition of $Ca_v1.3$ at 30 nM ($Ca_v1.3_L$, 75%; $Ca_v1.3_S$, 63%) but >90% inhibition at 300 nM. A 30 nM ISR concentration corresponds to a concentration at least 30-fold higher than the free plasma ISR concentrations reached during therapeutic dosing (see Discussion). As shown in Figure 8, *B* and *C*, 30 nM ISR did not measurably affect intracellular activity-related Ca^{2+} oscillations in the somata of SN DA neurons, which have been suggested to cause the high vulnerability of SN DA neurons to PD stressors (Guzman et al., 2010).

In summary, our data strongly suggest that supratherapeutic concentrations of ISR reduce neither pacemaker activity nor somatic Ca^{2+} transients in SN DA neurons, indicating that they are not sufficiently inhibiting LTCC activity.

Discussion

Our findings reveal a role of LTCCs in SN DA neurons that is relevant for PD pathophysiology in several important ways. We

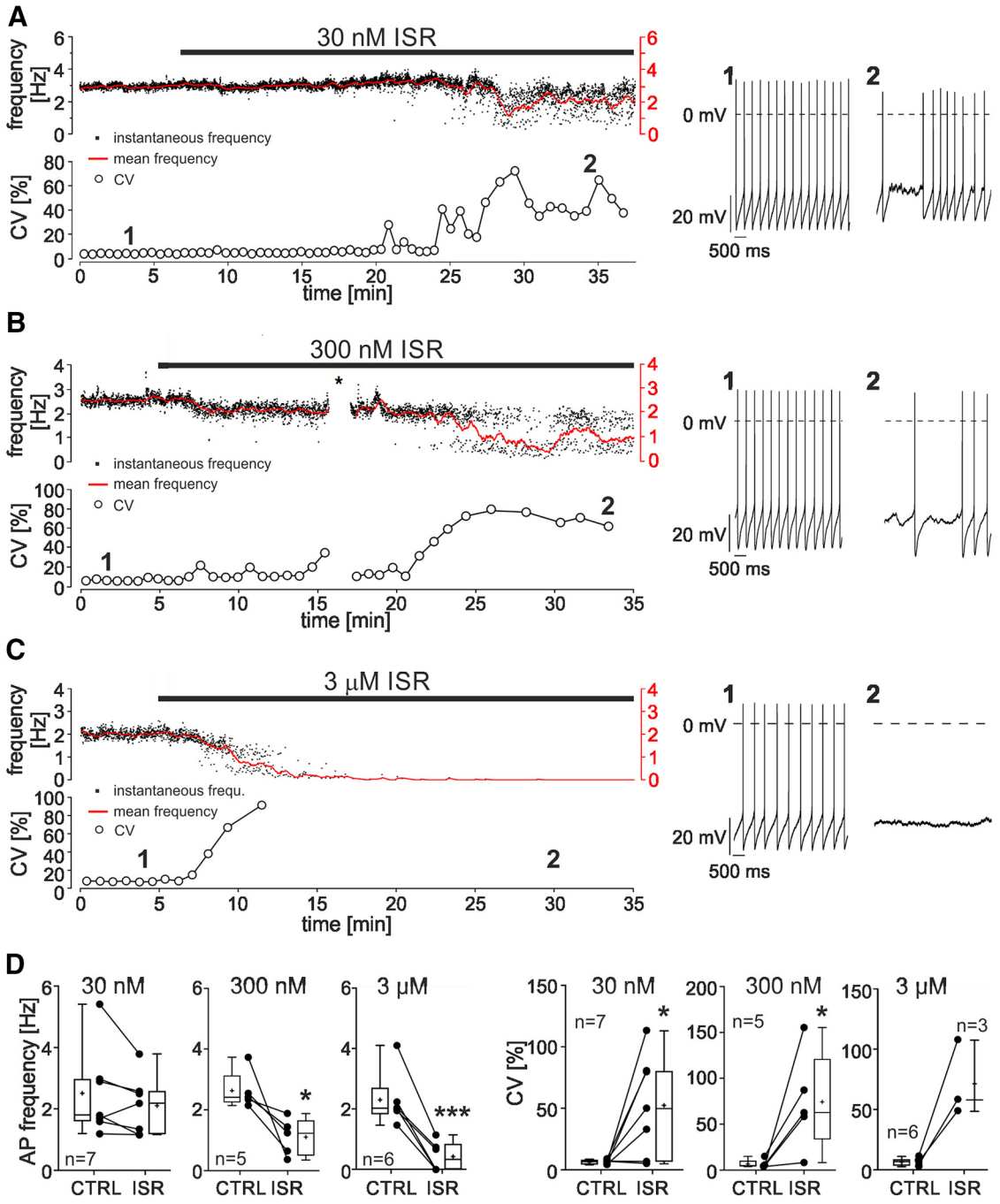

Figure 7. ISR effects on pacemaking in SN DA neurons recorded in adult mouse brain slices. ***A–C***, Top, ISR effect on instantaneous AP frequency (black dots, calculated from current ISI), mean AP frequency (red line, bin width 30 s), and CV (from 100 ISI) before and during application of the indicated concentrations of ISR. Original traces from the recordings at the time points indicated by numbers are shown on the right. ***D***, Summary box plots for spontaneous frequency and CV (mean of 2 min) under control conditions (CTRL) and 30 min after application of the indicated ISR concentrations (ISR). The number of neurons is given in the panels. After exposure to 3 μM ISR, three of six neurons stopped firing spontaneous APs and could not be included in the CV analysis. Statistical significance was determined using paired *t* test: ***$p < 0.001$; **$p < 0.01$; *$p < 0.05$. The asterisk in ***B*** shows a brief interruption of data acquisition.

demonstrate that under SN DA-like activity $Ca_v1.2$ and $Ca_v1.3$ splice variants contribute differentially to Ca^{2+} currents. $Ca_v1.3$ channels not only conducted Ca^{2+} between SN DA AP spikes and mediated increased Ca^{2+} influx during bursts but, unlike $Ca_v1.2$, also during APs following bursts. This identifies $Ca_v1.3$ as the molecular component mediating the low-threshold Ca^{2+} current described in SN DA neurons, which can contribute to pacemaking and low-threshold Ca^{2+} oscillations (Puopolo et al., 2007; Guzman et al., 2009; Khaliq and Bean, 2010; Hage and Khaliq, 2015; Evans et al., 2017). Although these observations propose that $Ca_v1.3$ could serve as a preferred target for neuroprotection with available DHP channel blockers (Surmeier et al., 2012; Duda et al., 2016), our findings challenge this view. First, we show that LTCCs during SN DA neuronal activity patterns require higher ISR concentrations for inhibition compared with aSM $Ca_v1.2$ channels, their cardiovascular drug target. Therefore, our data predict that less sensitive $Ca_v1.3$ channels would require 4.6- to 11.2-fold higher concentrations for inhibition, and there-

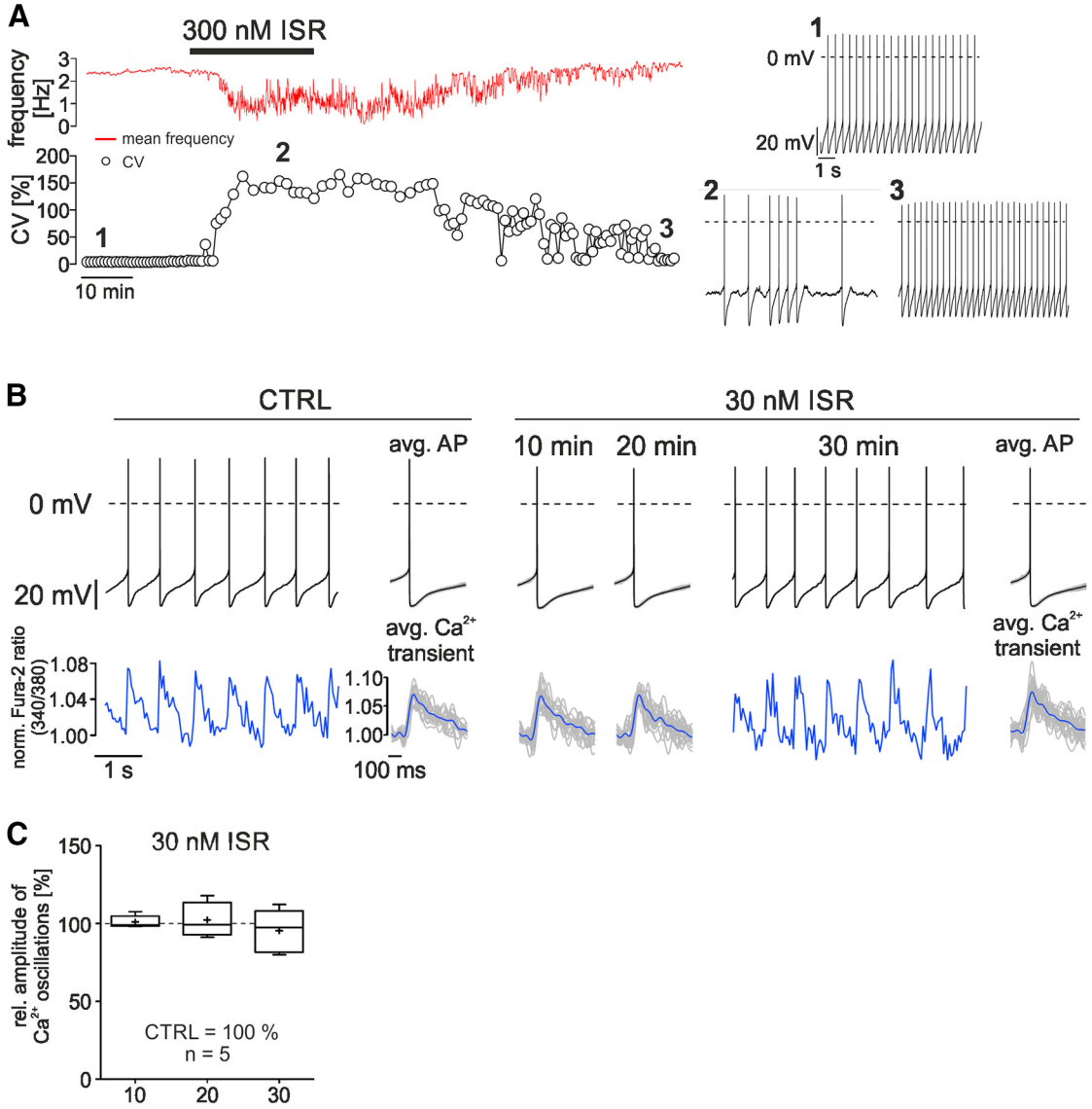

Figure 8. ISR effects on pacemaking and AP-associated Ca^{2+} oscillations. ***A***, Recording demonstrating the reversibility of pacemaking changes induced by 25 min perfusion with 300 nM ISR. Notice the different time scale of this recording compared with those in Figure 7. Original traces from the recordings shown above at the time points indicated by numbers are shown on the right. ***B***, Neurons were recorded in the perforated patch-clamp configuration (top traces), while somatic Ca^{2+} oscillations were simultaneously imaged (bottom traces). Since AP-associated Ca^{2+} dynamics are strongly frequency dependent, the AP frequency was adjusted for Ca^{2+} imaging in all recorded neurons to a similar value of ~1.5 Hz (mean ± SD, 1.48 ± 0.06 Hz; $n = 20$; five neurons, four time points in each neuron) by current clamp. The continuous recordings illustrate the AP firing and the associated somatic Ca^{2+} oscillations under control conditions (CTRL) and after 30 min of ISR application. The panels in between show the mean of 20 APs and the associated Ca^{2+} oscillations for the control (CTRL) and the indicated times after ISR application. Individual traces are superimposed in gray. They are barely visible for the APs due to small variability. ***C***, Summary box plot showing the amplitude of Ca^{2+} oscillations 10, 20, and 30 min after the application of 30 nM ISR. Mean amplitudes of 20 oscillations were calculated and normalized to the amplitude at time 0 (CTRL). Data for five neurons are shown. No significant change by ISR exposure was observed (five neurons, one-sample *t* test).

fore higher daily doses of ISR as currently used in an ongoing clinical trial. Our result that 30 nM ISR (a supratherapeutic concentration, see below) causes a much weaker inhibition of $Ca_v1.3$-driven pacemaking compared with concentrations of 300 nM and 3 μM, agrees with these findings. This lower sensitivity could also explain the absence of neuroprotection in our mouse 6-OHDA PD model by steady-state plasma ISR concentrations corresponding to those achieved during therapeutic dosing (3–4 ng/ml; see below). Second, we show that SN DA neuron survival upon 6-OHDA challenge was unaltered in $Ca_v1.3$-deficient mice. This suggests either that $Ca_v1.3$ does not significantly contribute to the high vulnerability of SN DA neurons or that chronic $Ca_v1.3$ deficiency-triggered compensatory mechanisms contribute to vulnerability, as reported previously (Poetschke et al., 2015). Our findings are of particular relevance in view of an ongoing clinical phase III trial assessing the neuroprotective effect of ISR in early PD (NCT02168842; www.clinicaltrials.com) and may explain the controversial findings of DHP-mediated neuroprotection in PD animal models.

Unlike less vulnerable ventral tegmental area (VTA) neurons, low-threshold somatodendritic Ca^{2+} oscillations and associated mitochondrial oxidative stress are observed only in vulnerable SN DA neurons and can be reduced *in vitro* by ISR, revealing a crucial role of LTCCs (Guzman et al., 2009, 2010). While VTA neurons conduct mainly subthreshold Na^+ currents (Khaliq and Bean, 2010), SN DA neurons exhibit prominent DHP-sensitive low-threshold Ca^{2+} currents during the ISI (Puopolo et al., 2007; Philippart et al., 2016; Evans et al., 2017; Sun et al., 2017). Our

data provide strong evidence that this current is mediated by $Ca_v1.3$ because $Ca_v1.2$ is not activated during the ISI (Figs. 3*D*, 6*A*). Our observations also predict that during sustained pacemaking only ~20% of the maximal LTCC current remains due to voltage- and Ca^{2+}-dependent inactivation (Fig. 3*C–F*). Thus, inactivation of LTCCs may represent an important physiological mechanism preventing excessive Ca^{2+} entry into SN DA neurons with low Ca^{2+} buffering capacity (Surmeier et al., 2012). We show that $Ca_v1.3$ conducts the most Ca^{2+} at subthreshold potentials and mediates Ca^{2+} influx during the burst as well as postburst APs, and $Ca_v1.3$, therefore, is a logical target for neuroprotection. However, our data demonstrate that during SN DA-like activity available DHP LTCC blockers are weaker inhibitors of $Ca_v1.3$ compared with $Ca_v1.2$, particularly the short $Ca_v1.3$ splice variant (5.8- or 11.2-fold less sensitive than $Ca_v1.2$ during SN DA-like or aSM-like activity, respectively). The lower IC_{50} of $Ca_v1.2$ for ISR inhibition under aSM-like activity predicts that at a given plasma concentration, not only brain $Ca_v1.2$, but particularly aSM $Ca_v1.2$ channels in resistance blood vessels will be inhibited more efficiently than $Ca_v1.3$ channels in SN DA cells.

A strength of our study is that our approach allowed us to estimate the therapeutic window by directly comparing ISR sensitivities of LTCCs under SN DA-like activity with $Ca_v1.2$ under aSM-like activity. For *in vitro* experiments, direct comparisons of IC_{50} values of DHP channel blockers with total therapeutic plasma concentrations are not meaningful because total plasma concentrations do not account for ~90% plasma protein binding of DHP LTCC blockers. However, due to the fast equilibrium of non-plasma protein-bound free ISR (Uchida et al., 1997) or nimodipine with the cerebrospinal fluid (CSF) (Allen et al., 1983; Kupsch et al., 1996; Uchida et al., 1997; Woodward et al., 1998), the equilibrium with the lipophilic plasma membrane compartments of the channels in the brain and in peripheral cardiovascular tissues must be similar. This justifies our approach and questions previous *in vitro* estimates of target engagement for ISR based on *in vivo* total plasma concentrations (Ilijic et al., 2011). In contrast, steady-state *in vivo* mouse plasma concentrations are a reliable parameter to predict drug exposure for comparison with therapeutically relevant plasma concentrations in humans. The mean maximal tolerable plasma concentrations of 10 mg sustained-release preparations, comparable to continuous administration through pellets or pumps in our mice, are within a range of 3–4 ng/ml [8–10 nM, SPC Lomir^R (compendium.ch/mpro/mnr/2604/html/); Park et al., 2009; Christensen et al., 2000]. This range was covered in our study, indicating that concentrations reached in humans during chronic therapy were not neuroprotective in our 6-OHDA PD mouse model.

Based on the above considerations (~90% plasma protein binding), a total plasma concentration of 10 nM corresponds to a free ISR concentration of approximately ≤1 nM in the plasma or CSF. We show that even a 30-fold higher concentration (30 nM) only partially inhibited $Ca_v1.3$-mediated effects on pacemaking. These data support our pharmacological findings (Fig. 5*B*), showing only a partial inhibition of $Ca_v1.3$ at 30 nM ($hCa_v1.3_L$, 75%; $hCa_v1.3_S$, 63%), whereas 300 nM ISR is predicted to inhibit >90% of $Ca_v1.3$ currents, which is in agreement with our observation that 300 nM ISR evoked a stronger effect on SN DA neuronal pacemaking under our recording conditions. We also present evidence that 30 nM ISR does not significantly reduce activity-dependent somatic intracellular Ca^{2+} oscillations, the presumed mechanism underlying DHP neuroprotection (Surmeier et al., 2011). Although L-type currents comprise a significant amount of Ca^{2+} currents in rodent SN DA neurons (Durante et al., 2004; Branch et al., 2014; Sun et al., 2017), it is unknown how much of the somatic Ca^{2+} oscillations are due to voltage-gated Ca^{2+} channel activity, particularly from LTCCs. However, our experiments show that therapeutically relevant, low-nanomolar ISR concentrations do not affect somatic Ca^{2+} oscillations and, therefore, do not reduce the potentially toxic Ca^{2+} load in the somata of SN DA neurons during AP firing.

In our PD mouse model, knockout of $Ca_v1.3$ provided no neuroprotection, a supportive argument that $Ca_v1.3$ channels are an unsuitable pharmacological target. However, based on our previous study (Poetschke et al., 2015), we cannot rule out a compensatory effect resulting from the upregulation of $Ca_v3.1$ T-type or other voltage-gated Ca^{2+} channels known to compensate for $Ca_v1.3$-dependent SN DA inhibitory D_2 autoreceptor responses. This $Ca_v1.3$-mediated (or $Ca_v3.1$-mediated) D_2 autoreceptor sensitization favoring autoinhibition of SN DA activity is likely protective for SN DA neurons (Duda et al., 2016) and may provide an alternative explanation for the heterogeneous findings addressing protective effects of LTCC inhibitors on SN DA neurons in PD models. It may further explain our unexpected finding of adult $Ca_v1.3^{-/-}$ mice possessing a lower number of SN DA neurons under control conditions, although this may result from neurodevelopmental deficits similar to those described for auditory pathway neurons in these mice (Hirtz et al., 2011).

Other *in vivo* neuroprotection studies of SN DA neurons with DHP channel blockers in PD animal models were largely based on data with supratherapeutic plasma concentrations (Kupsch et al., 1996; Ilijic et al., 2011). At these concentrations, unspecific *in vivo* effects particularly due to peripheral blood pressure lowering via inhibition of aSM $Ca_v1.2$ cannot be excluded (Busquet et al., 2008). Differences in DHP concentrations may, therefore, be one factor explaining why neuroprotection was observed in studies from two laboratories (Kupsch et al., 1995, 1996; Chan et al., 2007; Meredith et al., 2008; Ilijic et al., 2011) but could not be reproduced by us and others (Sautter et al., 1997). Other experimental variables must also be taken into account including age (young animals in Chan et al., 2007; Ilijic et al., 2011; adult mice in our study). Other studies failed to report DHP plasma concentrations (Kupsch et al., 1995) or were based on single experiments and low sample size (Kupsch et al., 1995, 1996; Ilijic et al., 2011). At present, a unifying factor explaining different outcomes in preclinical neuroprotection studies cannot be identified, but, as described here, insufficient inhibition of $Ca_v1.3$ channels may contribute to this finding.

In conclusion, LTCCs are implicated in various neurological human diseases (for review, see Striessnig et al., 2015), and reduction of $Ca_v1.3$-mediated Ca^{2+} entry is regarded as a promising neuroprotective approach, not only for PD. However, our findings predict that due to dose limitations, existing LTCC blockers fail to efficiently inhibit $Ca_v1.3$ LTCCs during neuronal activity in SN DA neurons. The therapeutic efficacy of this neuroprotective principle may, therefore, be underestimated with maximally tolerated ISR doses currently used in an ongoing phase III clinical trial.

References

Akaike N, Harata N (1994) Nystatin perforated patch recording and its applications to analyses of intracellular mechanisms. Jpn J Physiol 44:433–473. CrossRef Medline

Allen GS, Ahn HS, Preziosi TJ, Battye R, Boone SC, Boone SC, Chou SN, Kelly

DL, Weir BK, Crabbe RA, Lavik PJ, Rosenbloom SB, Dorsey FC, Ingram CR, Mellits DE, Bertsch LA, Boisvert DP, Hundley MB, Johnson RK, Strom JA, et al (1983) Cerebral arterial spasm–a controlled trial of nimodipine in patients with subarachnoid hemorrhage. N Engl J Med 308: 619–624. CrossRef Medline

Amini B, Clark JW Jr, Canavier CC (1999) Calcium dynamics underlying pacemaker-like and burst firing oscillations in midbrain dopaminergic neurons: a computational study. J Neurophysiol 82:2249–2261. Medline

Biel M, Hullin R, Freundner S, Singer D, Dascal N, Flockerzi V, Hofmann F (1991) Tissue-specific expression of high-voltage-activated dihydropyridine-sensitive L-type calcium channels. Eur J Biochem 200:81–88. CrossRef Medline

Bock G, Gebhart M, Scharinger A, Jangsangthong W, Busquet P, Poggiani C, Sartori S, Mangoni ME, Sinnegger-Brauns MJ, Herzig S, Striessnig J, Koschak A (2011) Functional properties of a newly identified C-terminal splice variant of Cav1.3 L-type Ca^{2+} channels. J Biol Chem 286:42736–42748. CrossRef Medline

Branch SY, Sharma R, Beckstead MJ (2014) Aging decreases L-type calcium channel currents and pacemaker firing fidelity in substantia nigra dopamine neurons. J Neurosci 34:9310–9318. CrossRef Medline

Busquet P, Hetzenauer A, Sinnegger-Brauns MJ, Striessnig J, Singewald N (2008) Role of L-type calcium channel isoforms in the extinction of conditioned fear. Learn Mem 15:378–386. CrossRef Medline

Catterall WA, Perez-Reyes E, Snutch TP, Striessnig J (2005) International Union of Pharmacology. XLVIII. Nomenclature and structure-function relationships of voltage-gated calcium channels. Pharmacol Rev 57:411–425. CrossRef Medline

Chan CS, Guzman JN, Ilijic E, Mercer JN, Rick C, Tkatch T, Meredith GE, Surmeier DJ (2007) "Rejuvenation" protects neurons in mouse models of Parkinson's disease. Nature 447:1081–1086. CrossRef Medline

Christensen HR, Antonsen K, Simonsen K, Lindekaer A, Bonde J, Angelo HR, Kampmann JP (2000) Bioavailability and pharmacokinetics of isradipine after oral and intravenous administration: half-life shorter than expected? Pharmacol Toxicol 86:178–182. CrossRef Medline

Costa KM (2014) The effects of aging on substantia nigra dopamine neurons. J Neurosci 34:15133–15134. CrossRef Medline

Davis MJ, Hill MA (1999) Signaling mechanisms underlying the vascular myogenic response. Physiol Rev 79:387–423. Medline

Destexhe A, Mainen ZF, Sejnowski TJ (1994) Synthesis of models for excitable membranes, synaptic transmission and neuromodulation using a common kinetic formalism. J Comput Neurosci 1:195–230. CrossRef Medline

Dodt HU, Zieglgänsberger W (1994) Infrared videomicroscopy: a new look at neuronal structure and function. Trends Neurosci 17:453–458. CrossRef Medline

Dougalis AG, Matthews GAC, Liss B, Ungless MA (2017) Ionic currents influencing spontaneous firing and pacemaker frequency in dopamine neurons of the ventrolateral periaqueductal gray and dorsal raphe nucleus (vlPAG/DRN): a voltage-clamp and computational modelling study. J Comput Neurosci 42:275–305. CrossRef Medline

Dragicevic E, Poetschke C, Duda J, Schlaudraff F, Lammel S, Schiemann J, Fauler M, Hetzel A, Watanabe M, Lujan R, Malenka RC, Striessnig J, Liss B (2014) Cav1.3 channels control D2-autoreceptor responses via NCS-1 in substantia nigra dopamine neurons. Brain 137:2287–2302. CrossRef Medline

Dragicevic E, Schiemann J, Liss B (2015) Dopamine midbrain neurons in health and Parkinson's disease: emerging roles of voltage-gated calcium channels and ATP-sensitive potassium channels. Neuroscience 284:798–814. CrossRef Medline

Drion G, Massotte L, Sepulchre R, Seutin V (2011) How modeling can reconcile apparently discrepant experimental results: the case of pacemaking in dopaminergic neurons. PLoS Comput Biol 7:e1002050. CrossRef Medline

Duda J, Potschke C, Liss B (2016) Converging roles of ion channels, calcium, metabolic stress, and activity-pattern of substantia nigra dopaminergic neurons in health and Parkinson's disease. J Neurochem 139 [Suppl 1]:156–178. CrossRef Medline

Durante P, Cardenas CG, Whittaker JA, Kitai ST, Scroggs RS (2004) Low-threshold L-type calcium channels in rat dopamine neurons. J Neurophysiol 91:1450–1454. CrossRef Medline

Evans RC, Zhu M, Khaliq ZM (2017) Dopamine inhibition differentially controls excitability of substantia nigra dopamine neuron subpopulations through T-type calcium channels. J Neurosci 37:3704–3720. CrossRef Medline

Fleischmann BK, Murray RK, Kotlikoff MI (1994) Voltage window for sustained elevation of cytosolic calcium in smooth muscle cells. Proc Natl Acad Sci U S A 91:11914–11918. CrossRef Medline

Grace AA, Bunney BS (1984a) The control of firing pattern in nigral dopamine neurons: single spike firing. J Neurosci 4:2866–2876. Medline

Grace AA, Bunney BS (1984b) The control of firing pattern in nigral dopamine neurons: burst firing. J Neurosci 4:2877–2890. Medline

Gründemann J, Schlaudraff F, Liss B (2011) UV-laser microdissection and mRNA expression analysis of individual neurons from postmortem Parkinson's disease brains. Methods Mol Biol 755:363–374. CrossRef Medline

Gundersen HJ, Jensen EB (1987) The efficiency of systematic sampling in stereology and its prediction. J Microsc 147:229–263. CrossRef Medline

Guzman JN, Sánchez-Padilla J, Chan CS, Surmeier DJ (2009) Robust pacemaking in substantia nigra dopaminergic neurons. J Neurosci 29:11011–11019. CrossRef Medline

Guzman JN, Sanchez-Padilla J, Wokosin D, Kondapalli J, Ilijic E, Schumacker PT, Surmeier DJ (2010) Oxidant stress evoked by pacemaking in dopaminergic neurons is attenuated by DJ-1. Nature 468:696–700. CrossRef Medline

Hage TA, Khaliq ZM (2015) Tonic firing rate controls dendritic Ca^{2+} signaling and synaptic gain in substantia nigra dopamine neurons. J Neurosci 35:5823–5836. CrossRef Medline

Helton TD, Xu W, Lipscombe D (2005) Neuronal L-type calcium channels open quickly and are inhibited slowly. J Neurosci 25:10247–10251. CrossRef Medline

Hess ME, Hess S, Meyer KD, Verhagen LA, Koch L, Brönneke HS, Dietrich MO, Jordan SD, Saletore Y, Elemento O, Belgardt BF, Franz T, Horvath TL, Rüther U, Jaffrey SR, Kloppenburg P, Brüning JC (2013) The fat mass and obesity associated gene (Fto) regulates activity of the dopaminergic midbrain circuitry. Nat Neurosci 16:1042–1048. CrossRef Medline

Hines ML, Carnevale NT (1997) The NEURON simulation environment. Neural Comput 9:1179–1209. CrossRef Medline

Hirtz JJ, Boesen M, Braun N, Deitmer JW, Kramer F, Lohr C, Müller B, Nothwang HG, Striessnig J, Löhrke S, Friauf E (2011) $Ca_v1.3$ calcium channels are required for normal development of the auditory brainstem. J Neurosci 31:8280–8294. CrossRef Medline

Hofmann F, Flockerzi V, Kahl S, Wegener JW (2014) L-type CaV1.2 calcium channels: from in vitro findings to in vivo function. Physiol Rev 94:303–326. CrossRef Medline

Horn R, Marty A (1988) Muscarinic activation of ionic currents measured by a new whole-cell recording method. J Gen Physiol 92:145–159. CrossRef Medline

Huang H, Yu D, Soong TW (2013) C-Terminal alternative splicing of CaV1.3 channels distinctively modulates their dihydropyridine sensitivity. Mol Pharmacol 84:643–653. CrossRef Medline

Huang H, Ng CY, Yu D, Zhai J, Lam Y, Soong TW (2014) Modest $Cav1.3_{42}$-selective inhibition by compound 8 is β-subunit dependent. Nat Commun 5:4481. CrossRef Medline

Hurley MJ, Dexter DT (2012) Voltage-gated calcium channels and Parkinson's disease. Pharmacol Ther 133:324–333. CrossRef Medline

Hurley MJ, Brandon B, Gentleman SM, Dexter DT (2013) Parkinson's disease is associated with altered expression of CaV1 channels and calcium-binding proteins. Brain 136:2077–2097. CrossRef Medline

Ilijic E, Guzman JN, Surmeier DJ (2011) The L-type channel antagonist isradipine is neuroprotective in a mouse model of Parkinson's disease. Neurobiol Dis 43:364–371. CrossRef Medline

Kang S, Cooper G, Dunne SF, Dusel B, Luan CH, Surmeier DJ, Silverman RB (2012) Cav1.3-selective L-type calcium channel antagonists as potential new therapeutics for Parkinson's disease. Nat Commun 3:1146. CrossRef Medline

Khaliq ZM, Bean BP (2010) Pacemaking in dopaminergic ventral tegmental area neurons: depolarizing drive from background and voltage-dependent sodium conductances. J Neurosci 30:7401–7413. CrossRef Medline

Komendantov AO, Komendantova OG, Johnson SW, Canavier CC (2004) A modeling study suggests complementary roles for GABAA and NMDA receptors and the SK channel in regulating the firing pattern in midbrain dopamine neurons. J Neurophysiol 91:346–357. CrossRef Medline

Koschak A, Reimer D, Huber I, Grabner M, Glossmann H, Engel J, Striessnig J (2001) alpha 1D (Cav1.3) subunits can form l-type Ca^{2+} channels

activating at negative voltages. J Biol Chem 276:22100–22106. CrossRef Medline

Koschak A, Reimer D, Walter D, Hoda JC, Heinzle T, Grabner M, Striessnig J (2003) $Ca_v1.4$alpha1 subunits can form slowly inactivating dihydropyridine-sensitive L-type Ca^{2+} channels lacking Ca^{2+}-dependent inactivation. J Neurosci 23: 6041–6049. Medline

Krabbe S, Duda J, Schiemann J, Poetschke C, Schneider G, Kandel ER, Liss B, Roeper J, Simpson EH (2015) Increased dopamine D2 receptor activity in the striatum alters the firing pattern of dopamine neurons in the ventral tegmental area. Proc Natl Acad Sci U S A 112:E1498–E1506. CrossRef Medline

Kupsch A, Gerlach M, Pupeter SC, Sautter J, Dirr A, Arnold G, Opitz W, Przuntek H, Riederer P, Oertel WH (1995) Pretreatment with nimodipine prevents MPTP-induced neurotoxicity at the nigral, but not at the striatal level in mice. Neuroreport 6:621–625. CrossRef Medline

Kupsch A, Sautter J, Schwarz J, Riederer P, Gerlach M, Oertel WH (1996) 1-Methyl-4-phenyl-1,2,3,6-tetrahydropyridine-induced neurotoxicity in non-human primates is antagonized by pretreatment with nimodipine at the nigral, but not at the striatal level. Brain Res 741:185–196. CrossRef Medline

Lacey MG, Mercuri NB, North RA (1989) Two cell types in rat substantia nigra zona compacta distinguished by membrane properties and the actions of dopamine and opioids. J Neurosci 9:1233–1241. Medline

Lacinová L, Klugbauer N, Hofmann F (2000) State- and isoform-dependent interaction of isradipine with the α_{1C} L-type calcium channel. Pflugers Arch 440:50–60. CrossRef Medline

Lieb A, Ortner N, Striessnig J (2014) C-terminal modulatory domain controls coupling of voltage-sensing to pore opening in Cav1.3 L-type Ca^{2+} channels. Biophys J 106:1467–1475. CrossRef Medline

Liss B, Franz O, Sewing S, Bruns R, Neuhoff H, Roeper J (2001) Tuning pacemaker frequency of individual dopaminergic neurons by Kv4.3L and KChip3.1 transcription. EMBO J 20:5715–5724. CrossRef Medline

Liss B, Haeckel O, Wildmann J, Miki T, Seino S, Roeper J (2005) K-ATP channels promote the differential degeneration of dopaminergic midbrain neurons. Nat Neurosci 8:1742–1751. CrossRef Medline

Marcantoni A, Vandael DH, Mahapatra S, Carabelli V, Sinnegger-Brauns MJ, Striessnig J, Carbone E (2010) Loss of Cav1.3 channels reveals the critical role of L-type and BK channel coupling in pacemaking mouse adrenal chromaffin cells. J Neurosci 30:491–504. CrossRef Medline

Mercuri NB, Bonci A, Calabresi P, Stratta F, Stefani A, Bernardi G (1994) Effects of dihydropyridine calcium antagonists on rat midbrain dopaminergic neurones. Br J Pharmacol 113:831–838. CrossRef Medline

Meredith GE, Totterdell S, Potashkin JA, Surmeier DJ (2008) Modeling PD pathogenesis in mice: advantages of a chronic MPTP protocol. Parkinsonism Relat Disord 14 [Suppl 2]:S112–S115. CrossRef Medline

Moosmang S, Schulla V, Welling A, Feil R, Feil S, Wegener JW, Hofmann F, Klugbauer N (2003) Dominant role of smooth muscle L-type calcium channel Cav1.2 for blood pressure regulation. EMBO J 22:6027–6034. CrossRef Medline

Nedergaard S, Flatman JA, Engberg I (1993) Nifedipine- and omega-conotoxin-sensitive Calcium conductances in guinea-pig substantia nigra pars compacta neurones. J Physiol 466:727–747. Medline

Olson PA, Tkatch T, Hernandez-Lopez S, Ulrich S, Ilijic E, Mugnaini E, Zhang H, Bezprozvanny I, Surmeier DJ (2005) G-protein-coupled receptor modulation of striatal $Ca_V1.3$ L-type Ca^{2+} channels is dependent on a Shank-binding domain. J Neurosci 25:1050–1062. CrossRef Medline

Ortner NJ, Bock G, Vandael DH, Mauersberger R, Draheim HJ, Gust R, Carbone E, Tuluc P, Striessnig J (2014) Pyrimidine-2,4,6-triones are a new class of voltage-gated L-type Ca^{2+} channel activators. Nat Commun 5:3897. CrossRef Medline

Paladini CA, Roeper J (2014) Generating bursts (and pauses) in the dopamine midbrain neurons. Neuroscience 282:109–121. CrossRef Medline

Park JH, Park YS, Rhim SY, Jhee OH, Kim SH, Yang SC, Lee MH, Shaw LM, Kang JS (2009) Quantification of isradipine in human plasma using LC-MS/MS for pharmacokinetic and bioequivalence study. J Chromatogr B Analyt Technol Biomed Life Sci 877:59–64. CrossRef Medline

Parkinson Study Group (2013) Phase II safety, tolerability, and dose selection study of isradipine as a potential disease-modifying intervention in early Parkinson's disease (STEADY-PD). Mov Disord 28:1823–1831. CrossRef Medline

Patil PG, Brody DL, Yue DT (1998) Preferential closed-state inactivation of neuronal calcium channels. Neuron 20:1027–1038. CrossRef Medline

Paxinos G, Franklin KBJ (2001) Paxinos and Franklin's the mouse brain in stereotaxic coordinates. San Diego, CA: Academic.

Philippart F, Destreel G, Merino-Sepúlveda P, Henny P, Engel D, Seutin V (2016) Differential somatic Ca^{2+} channel profile in midbrain dopaminergic neurons. J Neurosci 36:7234–7245. CrossRef Medline

Platzer J, Engel J, Schrott-Fischer A, Stephan K, Bova S, Chen H, Zheng H, Striessnig J (2000) Congenital deafness and sinoatrial node dysfunction in mice lacking class D L-type Ca^{2+} channels. Cell 102:89–97. CrossRef Medline

Poetschke C, Dragicevic E, Duda J, Benkert J, Dougalis A, DeZio R, Snutch TP, Striessnig J, Liss B (2015) Compensatory T-type Ca^{2+} channel activity alters D2-autoreceptor responses of Substantia nigra dopamine neurons from Cav1.3 L-type Ca^{2+} channel KO mice. Sci Rep 5:13688. CrossRef Medline

Puopolo M, Raviola E, Bean BP (2007) Roles of subthreshold calcium current and sodium current in spontaneous firing of mouse midbrain dopamine neurons. J Neurosci 27:645–656. CrossRef Medline

Putzier I, Kullmann PH, Horn JP, Levitan ES (2009) $Ca_v1.3$ channel voltage dependence, not Ca^{2+} selectivity, drives pacemaker activity and amplifies bursts in nigral dopamine neurons. J Neurosci 29:15414–15419. CrossRef Medline

Richards CD, Shiroyama T, Kitai ST (1997) Electrophysiological and immunocytochemical characterization of GABA and dopamine neurons in the substantia nigra of the rat. Neuroscience 80:545–557. CrossRef Medline

Sautter J, Kupsch A, Earl CD, Oertel WH (1997) Degeneration of prelabelled nigral neurons induced by intrastriatal 6-hydroxydopamine in the rat: behavioural and biochemical changes and pretreatment with the calcium-entry blocker nimodipine. Exp Brain Res 117:111–119. CrossRef Medline

Schiemann J, Schlaudraff F, Klose V, Bingmer M, Seino S, Magill PJ, Zaghloul KA, Schneider G, Liss B, Roeper J (2012) K-ATP channels in dopamine substantia nigra neurons control bursting and novelty-induced exploration. Nat Neurosci 15:1272–1280. CrossRef Medline

Snutch TP, Tomlinson WJ, Leonard JP, Gilbert MM (1991) Distinct calcium channels are generated by alternative splicing and are differentially expressed in the mammalian CNS. Neuron 7:45–57. CrossRef Medline

Soldatov NM, Bouron A, Reuter H (1995) Different voltage-dependent inhibition by dihydropyridines of human Ca^{2+} channel splice variants. J Biol Chem 270:10540–10543. CrossRef Medline

Striessnig J, Pinggera A, Kaur G, Bock G, Tuluc P (2014) L-type Ca^{2+} channels in heart and brain. Wiley Interdiscip Rev Membr Transp Signal 3:15–38. CrossRef Medline

Striessnig J, Ortner NJ, Pinggera A (2015) Pharmacology of L-type calcium channels: novel drugs for old targets? Curr Mol Pharmacol 8:110–122. CrossRef Medline

Sulzer D, Surmeier DJ (2013) Neuronal vulnerability, pathogenesis, and Parkinson's disease. Mov Disord 28:41–50. CrossRef Medline

Sun Y, Zhang H, Selvaraj S, Sukumaran P, Lei S, Birnbaumer L, Singh BB (2017) Inhibition of L-type Ca^{2+} channels by TRPC1-STIM1 complex is essential for the protection of dopaminergic neurons. J Neurosci 37: 3364–3377. CrossRef Medline

Surmeier DJ, Guzman JN, Sanchez-Padilla J, Goldberg JA (2011) The origins of oxidant stress in Parkinson's disease and therapeutic strategies. Antioxid Redox Signal 14:1289–1301. CrossRef Medline

Surmeier DJ, Guzman JN, Sanchez J, Schumacker PT (2012) Physiological phenotype and vulnerability in Parkinson's disease. Cold Spring Harb Perspect Med 2:a009290. CrossRef Medline

Tan BZ, Jiang F, Tan MY, Yu D, Huang H, Shen Y, Soong TW (2011) Functional characterization of alternative splicing in the C terminus of L-type CaV1.3 channels. J Biol Chem 286:42725–42735. CrossRef Medline

Uchida S, Yamada S, Nagai K, Deguchi Y, Kimura R (1997) Brain pharmacokinetics and in vivo receptor binding of 1,4-dihydropyridine calcium channel antagonists. Life Sci 61:2083–2090. CrossRef Medline

Ungless MA, Whistler JL, Malenka RC, Bonci A (2001) Single cocaine exposure in vivo induces long-term potentiation in dopamine neurons. Nature 411:583–587. CrossRef Medline

Wang Y, Jin Z, Wang Z, Jiang X, Wang L (2013) Pharmacokinetic properties of isradipine after single-dose and multiple-dose oral administration in Chinese volunteers: a randomized, open-label, parallel-group phase I study. Biomed Chromatogr 27:1664–1670. CrossRef Medline

Welling A, Ludwig A, Zimmer S, Klugbauer N, Flockerzi V, Hofmann F (1997) Alternatively spliced IS6 segments of the α1C gene determine the tissue-specific dihydropyridine sensitivity of cardiac and vascular smooth muscle L-type Ca^{2+} channels. Circ Res 81:526–532. CrossRef Medline

Woodward DK, Hatton J, Ensom MH, Young B, Dempsey R, Clifton GD (1998) Alpha1-acid glycoprotein concentrations and cerebrospinal fluid drug distribution after subarachnoid hemorrhage. Pharmacotherapy 18: 1062–1068. Medline

Xu W, Lipscombe D (2001) Neuronal $Ca_v1.3\alpha1$ L-type channels activate at relatively hyperpolarized membrane potentials and are incompletely inhibited by dihydropyridines. J Neurosci 21:5944–5951. Medline

Ye JH, Zhang J, Xiao C, Kong JQ (2006) Patch-clamp studies in the CNS illustrate a simple new method for obtaining viable neurons in rat brain slices: glycerol replacement of NaCl protects CNS neurons. J Neurosci Methods 158:251–259. CrossRef Medline

Zamponi GW, Striessnig J, Koschak A, Dolphin AC (2015) The physiology, pathology, and pharmacology of voltage-gated calcium channels and their future therapeutic potential. Pharmacol Rev 67:821–870. CrossRef Medline

Zhang J, Berra-Romani R, Sinnegger-Brauns MJ, Striessnig J, Blaustein MP, Matteson DR (2007) Role of Cav1.2 L-type Ca^{2+} channels in vascular tone: effects of nifedipine and Mg^{2+}. Am J Physiol Heart Circ Physiol 292:H415–H425. CrossRef Medline

Zühlke RD, Bouron A, Soldatov NM, Reuter H (1998) Ca^{2+} channel sensitivity toward the blocker isradipine is affected by alternative splicing of the human alpha1C subunit gene. FEBS Lett 427:220–224. CrossRef Medline